Draft version September 2, 2025
Typeset using LaTeX **twocolumn** style in AASTeX631

The Effect of Different Methods for Accounting for α-enhancement on the Asteroseismic Modeling of Metal-Poor Stars

Christopher J. Lindsay [1], J. M. Joel Ong (王加冕) [2,3], Sarbani Basu [1], Samuel Grunblatt [4], and Marc Hon [5]

[1] *Department of Astronomy, Yale University, PO Box 208101, New Haven, CT 06520-8101, USA*
[2] *Institute for Astronomy, University of Hawai'i, 2680 Woodlawn Drive, Honolulu, HI 96822, USA*
[3] *Hubble Fellow*
[4] *Department of Physics and Astronomy, University of Alabama, 514 University Drive, Tuscaloosa, AL 35487-0324, USA*
[5] *Kavli Institute for Astrophysics and Space Research, Massachusetts Institute of Technology, Cambridge, MA 02139, USA*

ABSTRACT

Constraining stellar models using asteroseismic and spectroscopic observations is a powerful method for precisely determining the fundamental properties of stars in different kinematic components of our galaxy. We use spectroscopy, and individual oscillation mode frequencies, of eight evolved metal-poor stars enhanced in α-elements to perform a homogeneous modeling study of these stars. We compare a full treatment of α-enhancement, against an ad hoc correction to the total metallicity. We show that the stellar properties inferred from both sets of models agree with each other, although the uncertainties on stellar parameters derived from the full α-enhanced modeling are slightly smaller. This is in qualitative disagreement with existing works showing inferred red-giant ages to depend strongly on the opacities and abundances assumed in 1D modeling. Comparing our constraints on stellar properties against those based only on the global asteroseismic parameters, we find that the observed frequency of maximum oscillation power ($\nu_{\rm max}$) is larger than the value inferred from applying the $\nu_{\rm max}$ scaling relation to the masses, radii, and temperature results derived from our detailed modeling. This discrepancy is more pronounced at low metallicities, consistent with recent findings indicating a breakdown of the $\nu_{\rm max}$ scaling relation for metal-poor stars. Understanding the extent to which the $\nu_{\rm max}$ scaling relation fails for low-metallicity solar-like oscillators through detailed modeling will enable more accurate mass and age determinations for hundreds of giant stars in the Galactic Halo for which only global asteroseismic parameters are available.

Keywords: asteroseismology - stars: solar-type - stars: oscillations - Galaxy: halo - Galaxy: formation

1. INTRODUCTION

Combined position and velocity measurements from *Gaia* (Gaia Collaboration et al. 2016, 2018, 2021), and spectroscopic abundance data from experiments like APOGEE (S. R. Majewski et al. 2016), have enabled the detailed study of substructure in the Milky Way's Halo. This rich substructure in turn evinces the complex, hierarchical history of structure formation in the Milky Way. In order to determine when merger events occurred, and study the properties of the smaller galaxies that merged with the Milky Way, it is vital to determine ages for stars in the Halo. The age-dating of halo stellar populations associated with merger events has been carried out extensively for this purpose by comparing the spectroscopic qualities of stars in these populations to grids of stellar isochrones (e.g. H. H. Koppelman et al. 2019; M. Xiang & H.-W. Rix 2022; T. Ruiz-Lara et al. 2022; C. Gallart et al. 2024).

Asteroseismic observations taken by space-based missions — such as CoRoT (A. Baglin et al. 2006), *Kepler* (W. J. Borucki et al. 2010) and TESS (G. R. Ricker et al. 2015) — have previously been used, together with stellar spectra, to place precise constraints on the fundamental stellar parameters of thousands of stars (e.g. M. H. Pinsonneault et al. 2018, 2025; C. Marasco et al. 2025). Stars with outer convective envelopes, like our Sun, subgiants, and evolved giant stars, pulsate in many oscillation modes simultaneously. The stochastically-excited oscillations of these 'solar-like' oscillators produce peaks in power spectra that are obtained by taking the Fourier transform of a star's light curve (see S. Hekker & J. Christensen-Dalsgaard 2017, for a recent review of giant star asteroseismology). These oscillation peaks produce a comb-like pattern of regularly spaced pressure modes

Corresponding author: Christopher Lindsay
christopher.lindsay@yale.edu

since modes with the same angular degree, ℓ, show a consistent frequency spacing between overtones called the large frequency separation, $\Delta\nu$ (M. Tassoul 1980). $\Delta\nu$ scales with the square root of the stellar density. The oscillation peaks do not all have the same strength; instead, they appear under a Gaussian-like envelope with the peak of the envelope, called the frequency of maximum oscillation power or $\nu_{\rm max}$, scaling with the star's surface gravity and temperature (H. Kjeldsen & T. R. Bedding 1995; S. Basu & W. J. Chaplin 2017). Using these global asteroseismic scaling relations with measurements of temperature, $\Delta\nu$, and $\nu_{\rm max}$ directly return stellar masses and radii. Combining asteroseismic mass and radius determinations with stellar models permits more precise field star age determinations than are possible without the use of asteroseismology (D. R. Soderblom 2010, 2014). When individual mode frequencies can be determined from observed stellar power spectra, comparing the observed mode frequencies with theoretical oscillation mode frequencies predicted by stellar models provides constraints on stellar interior structure and enables more precise determinations of global parameters such as age.

Asteroseismic Galactic archaeology studies on a large scale have previously been carried out using global asteroseismic measurements derived from *Kepler* or CoRoT data (e.g. V. Silva Aguirre et al. 2018; A. Miglio et al. 2021; J. T. Warfield et al. 2021, 2024; A. Stokholm et al. 2023), and now are done using the large influx of data from TESS (e.g. S. K. Grunblatt et al. 2021; C. C. Borre et al. 2022; C. Marasco et al. 2025). The asteroseismic analyses of stars in different kinematic components of the Milky Way have thus far primarily relied on the global asteroseismic scaling relations to determine stellar masses and radii, and thereby ages through stellar models. However, recent work indicates that scaling relation-derived stellar parameters diverge from detailed asteroseismic modeling results, obtained by fitting the observed mode frequencies to the mode frequencies of stellar models (D. Huber et al. 2024; J. R. Larsen et al. 2025; C. J. Lindsay et al. 2025).

Accurate and precise stellar ages for metal-poor stars in the Galactic Halo are vital for determining the merger history of our galaxy. For example, a precise age determination for the metal-poor Halo star ν Indi (by W. J. Chaplin et al. 2020) placed a limit on the timing of the Gaia-Enceladus merger event, which is largely responsible for the formation of the inner Galactic Halo and Thick Disk (A. Helmi et al. 2018). More recently, C. J. Lindsay et al. (2025) also used individual mode frequency asteroseismic modeling to place a lower bound on when stars began to form in the dwarf galaxy progenitor of the Helmi streams (A. Helmi et al. 1999). Asteroseismology with individual mode frequencies remains the gold standard for determining precise stellar ages. However, modeling uncertainties such as the structural resolution of the models, mixing near convective boundaries, and treatments for non-solar elemental mixtures must now be explored (Y. Li & M. Joyce 2025; C. J. Lindsay et al. 2024).

In this work, we explore the effects of using different ways of treating α-element enhancement on asteroseismic stellar modeling. Metal-poor Halo stars are often enhanced in α elements compared with the Sun. These α elements form predominantly through the α-process and have mass numbers that are multiples of 4, including C, O, Ne, Mg, etc. They are so enhanced due to the early metal enrichment of the interstellar medium being the result of core-collapse supernovae, which produce higher concentrations of α-elements (M. Spite & F. Spite 1978; B. M. Tinsley 1980; A. McWilliam et al. 1995; P. E. Nissen & W. J. Schuster 2010; C. Kobayashi et al. 2020). Therefore, the Milky Way's old stars are enhanced in these α-elements when compared with younger stars like our Sun. Despite this, α-enhanced stars are often not generally studied using models that account for deviations from Solar elemental abundance patterns. Instead, the stars are often modeled using solar-scaled metallicities, with an empirical correction applied to the measured global metallicity (M. Salaris et al. 1993),

$$[\mathrm{Fe/H}]_{\rm corr} \simeq [\mathrm{Fe/H}]_{\rm orig} + \log_{10}(0.638 \times 10^{[\alpha/\mathrm{Fe}]} + 0.362). \quad (1)$$

The use of Equation 1 (which we will subsequently call the Salaris correction) allows for the construction of stellar evolutionary tracks that match a star's position in the HR diagram. Figure 1 illustrates this by comparing how evolutionary tracks of stellar models, calculated with the MESA stellar evolution code (B. Paxton et al. 2011, 2013, 2015, 2018, 2019; A. S. Jermyn et al. 2023), respond to these treatments of α-enhancement (see also T. Sun et al. 2023). At 0.85 solar masses, the α-enhanced track (gray line in Figure 1), calculated using α-enhanced element mixtures and opacity tables, lies at a lower temperature compared with the uncorrected track (blue line in Figure 1). Although the α-enhanced and uncorrected track both have the same initial iron abundance of $[\mathrm{Fe/H}]_0$ = -0.22, the initial global metal mass abundances (Z_0) differ due to the different elemental mixture. The Salaris-corrected track (orange line in Figure 1), calculated using a solar-scaled element mixture and solar-scaled opacity tables, mostly coincides with the α-enhanced track since it has a different $[\mathrm{Fe/H}]_0$, but exactly the same Z_0.

The internal structure of such an α-enhanced stellar model may not necessarily match that of an equivalent Salaris-corrected model constructed using solar-scaled abundances and opacities. As a result, the detailed asteroseismic properties and mode frequencies of α-enhanced and Salaris-corrected models may not reproduce each other, either. Structural and asteroseismic differences may in turn lead to discrepancies in stellar properties inferred from asteroseismology using Salaris-corrected models compared to those

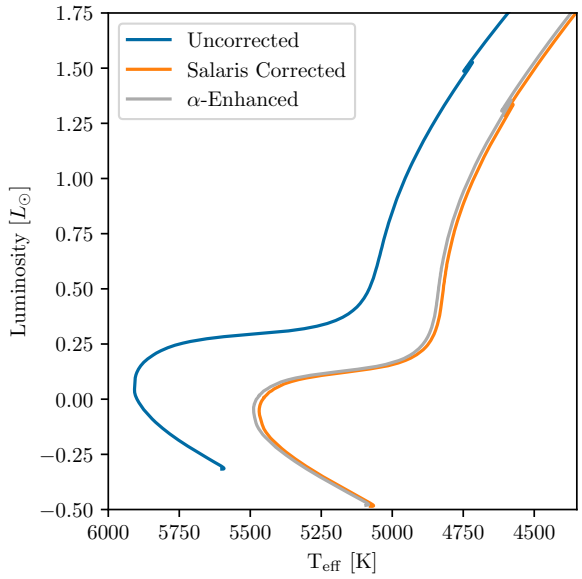

Figure 1. HR-Diagram evolutionary tracks, showing how stellar evolution changes when modeling stars that are enhanced in α-elements. The uncorrected track (blue line) shows the evolution of a 0.85 $M_\odot$ star with initial helium abundance Y_0 = 0.276 and initial iron abundance $[Fe/H]_0$ = -0.22. The α-enhanced track (gray line) has the same values of mass, Y_0, and $[Fe/H]_0$ as the uncorrected track but incorporates an α-enhancement factor of $[\alpha/Fe]$ = 0.4. The Salaris-corrected track (orange line) has a different $[Fe/H]_0$ value than the uncorrected track and instead matches the initial global metallicity (Z_0) of the α-enhanced track, while keeping the same solar-scaled (N. Grevesse & A. J. Sauval 1998) element abundance mixtures as the uncorrected track.

obtained using properly α-enhanced ones. Some existing works suggest that these discrepancies may be nontrivial. For example, Z. S. Ge et al. (2015) performed a grid-based modeling study of the evolved subgiant KIC7976303 and found the α-enhanced models fit the individual observed frequencies better than models constructed without α-enhancement, and that α-enhanced modeling implied a larger mass and younger age for the star compared with non-α-enhanced modeling. On the other hand, Z. S. Ge et al. (2015) also found that both α-enhanced and solar-scaled models matched the observations of KIC8694723. G. Valle et al. (2024) also found that using solar-scaled abundances and opacities in their grid-based stellar modeling led to biased ages. However, this latter work only used the global asteroseismic parameters, ν_{max} and $\Delta\nu$. In any case, it is difficult to assess how important α-enhanced modeling might be for asteroseismic inference by generalizing only this handful of studies.

Therefore, in this work, we seek to examine these potential α-enrichment modeling systematic effects more closely. We build on previous studies of α-enhanced asteroseismic stellar modeling by conducting a homogeneous modeling study of 8 metal-poor, α-enhanced stars, separately fitting α-enhanced and Salaris-corrected stellar models to each star based on combined constraints from spectroscopic observables and individual oscillation mode frequencies. Our goal in this work is to determine whether applying a full treatment of α-enhancement (altering abundance fractions and using opacity tables) significantly influences the stellar parameters estimated from asteroseismic modeling. We introduce our sample of 8 metal-poor, α-enhanced stars we study in the work in section 2 and describe the sources of the spectroscopic and asteroseismic data used in the modeling. We detail our asteroseismic modeling methods in section 3. The modeling results obtained using the different methods of accounting for α-enhancement are compared in section 4 and implications of the modeling results on metal-poor, α-enhanced asteroseismic stellar modeling are discussed in section 5.

2. THE SAMPLE

We perform detailed asteroseismic modeling on a sample of 8 metal-poor stars, all of which are enhanced to varying degrees in α-elements relative to the Sun. We report the values of effective temperature (T_{eff}), [Fe/H], [α/Fe], and luminosity (L) we use in our modeling in Table 1, along with their associated sources. The global asteroseismic parameters, $\Delta\nu$ and ν_{max}, are also reported in Table 1, although they are not directly included in our modeling procedure (see section 3). The observed [Fe/H] and [α/Fe] measurements show that the stars in our sample are all metal poor ([Fe/H] $\lesssim$ 1.5) and enhanced in α elements (0.15 $\lesssim$ [α/Fe] $\lesssim$ 0.4). Figure 2 shows our sample of stars as colored points in [Fe/H] versus [α/Fe] space, with the background points showing the observed [α/Fe] and [Fe/H] APOGEE DR17 (Abdurro'uf et al. 2022) measurements taken from the APOKASC-3 sample (M. H. Pinsonneault et al. 2025). The solid-colored points show the observed [Fe/H] measurements listed in Table 1, while the empty points show the [Fe/H] values after applying Equation 1.

Since our goal is to determine how the treatment of α-enhancement affects the asteroseismic modeling of evolved metal-poor stars through a homogeneous modeling effort, we build on previous studies that determined the asteroseismic mode frequencies for the target stars and used them to determine the fundamental parameters of the stars. 7 of the 8 stars have been studied using individual mode asteroseismology previously, including HD 128279 (C. J. Lindsay et al. 2025), HD 140283 (Lundkvist et al. (submitted)), HD 175305 (C. J. Lindsay et al. 2025), KIC 4671239 (J. R. Larsen et al. 2025), KIC 7341231 (S. Deheuvels & E. Michel 2011), KIC 8144907 (D. Huber et al. 2024), and ν Indi (W. J. Chaplin et al. 2020). In the case of ν Indi, additional higher-cadence TESS data has become available since the analysis of W. J. Chaplin et al. (2020), so we determine additional mode frequencies by applying PBJam (M. B. Nielsen et al.

Table 1. Spectroscopic and global asteroseismic observed values (with sources) of the 8 metal-poor stars in our sample. In cases where [α/Fe] were not reported explicitly in the literature, we determine [α/Fe] by taking an average of the observed α element abundances, weighted by the reported uncertainties. When luminosities from Gaia DR2 (Gaia Collaboration et al. 2018) are used, we adopt a conservative 15% error on L due to the negligibly small reported errors from the pipeline and strong degeneracy between effective temperature and reddening when using the Gaia broad band photometry.

Target	$T_{\rm eff}$ [K]	[Fe/H]	[α/Fe]	[Fe/H]$_{\rm corr}$	L [$L_\odot$]	$\Delta\nu$ [μHz]	$\nu_{\rm max}$ [μHz]
HD 128279	5328 ± 200^{a}	-2.17 ± 0.12^{a}	0.30^{a}	-1.95 ± 0.12	11.03 ± 1.124^{b}	15.87 ± 0.05^{b}	189.10 ± 0.5^{b}
HD 140283	5792 ± 55^{c}	-2.29 ± 0.14^{c}	0.40^{c}	-2.03 ± 0.14	4.77 ± 0.055^{c}	39.47 ± 0.05^{d}	611.30 ± 7.4^{d}
HD 175305	5036 ± 200^{a}	-1.35 ± 0.15^{a}	0.23^{a}	-1.19 ± 0.15	33.10 ± 3.0^{b}	5.89 ± 0.01^{b}	52.17 ± 0.4^{b}
KIC 4671239	5295 ± 145^{e}	-2.63 ± 0.20^{e}	0.13^{e}	-2.55 ± 0.20	16.78 ± 2.44^{f}	9.82 ± 0.05^{g}	98.9 ± 1.2^{g}
KIC 7341231	5233 ± 100^{h}	-1.64 ± 0.10^{h}	0.27^{i}	-1.45 ± 0.10	5.26 ± 0.79^{h}	28.9 ± 0.20^{h}	406.0 ± 3.0^{h}
KIC 8144907	5400 ± 200^{j}	-2.66 ± 0.08^{j}	0.38^{j}	-2.38 ± 0.08	11.13 ± 0.45^{j}	17.47 ± 0.09^{k}	208.2 ± 1.1^{k}
ν Indi	5320 ± 64^{l}	-1.43 ± 0.09^{l}	0.40^{l}	-1.18 ± 0.09	6.00 ± 0.35^{f}	$25.05 \pm 0.21^{*}$	$350.0 \pm 1.1^{*}$
TIC 300085386	5211 ± 55^{m}	-1.29 ± 0.10^{m}	0.29^{m}	-1.08 ± 0.10	20.89 ± 3.13^{f}	$6.62 \pm 0.06^{*}$	$60.13 \pm 3.0^{*}$

Sources: [a]M. N. Ishigaki et al. (2012); [b]C. J. Lindsay et al. (2025); [c]I. Karovicova et al. (2020); [d]Lundkvist et al. (submitted); [e]A. Alencastro Puls et al. (2022); [f] Gaia Collaboration et al. (2018); [g]J. R. Larsen et al. (2025); [h]S. Deheuvels et al. (2012); [i]APOGEE DR16 S. R. Majewski et al. (2016), J. C. Wilson et al. (2019); [j]D. Huber et al. (2024); [k]J. Yu et al. (2018); [l]W. J. Chaplin et al. (2020); [m]D. de Brito Silva et al. (2024); [*]This Work.

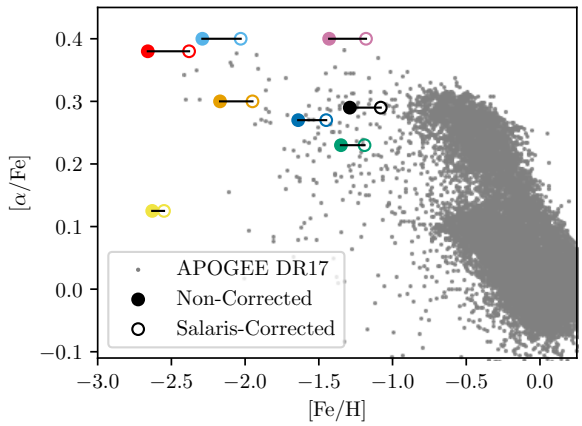

Figure 2. The observed [Fe/H] (filled symbols) and Salaris-corrected [Fe/H] (open symbols) values against the [α/Fe] measurements for the stars in our sample. The background small points show the distribution of stars in the APOKASC-3 sample in the [α/Fe]-[Fe/H] plane. The filled points show the [Fe/H] values for HD 128279 (orange), HD 140283 (light blue), HD 175305 (green), KIC 4671239 (yellow), KIC 7341231 (dark blue), KIC 8144907 (red), ν Indi (pink), and TIC 300085386 (black), while the open symbols show the [Fe/H] values after the correction from M. Salaris et al. (1993) is applied. These values are also listed in Table 1

2021) to all the available data (see Appendix A). Since TIC 300085386 has not been studied with detailed asteroseismology previously, we determine the oscillation mode frequencies in this work following the same method as described in C. J. Lindsay et al. (2025) (see Appendix B). In all other cases, we use the individual mode frequencies and errors reported in the previously mentioned corresponding papers in our modeling.

3. MODELING METHODS

Using the spectroscopic and asteroseismic input data described in section 2 we calculate many stellar model tracks for each target star using a similar iterative process to the method described in C. J. Lindsay et al. (2025). We use the differential evolution algorithm implemented in `yabox` (P. R. Mier 2017) to minimize a cost function representing the fit between the observed and model spectroscopic and asteroseismic properties. We do this, as opposed to grid-based modeling, in order to more densely sample the parameter space around the optimal model parameters. For each cost function evaluation, we first construct a stellar model evolution track using MESA version r22.05.1 (B. Paxton et al. 2011, 2013, 2015, 2018, 2019; A. S. Jermyn et al. 2023). The 4 model parameters varied over the course of the differential evolution optimization are initial mass (M_0), initial helium abundance (Y_0), initial metal abundance divided by initial hydrogen abundance ($f = Z_0/X_0$), and convective mixing length ($\alpha_{\rm mlt}$). The parameters are varied in the following ranges: $0.7 \leq M_0 \leq 1.0$, $0.245 \leq Y_0 \leq 0.27$, $0.00001 \leq f \leq 0.003$, and $1.6 \leq \alpha_{\rm mlt} \leq 2.0$.

Each track is computed from the pre-main-sequence until the point along the red giant branch where the model's luminosity is significantly higher ($\gtrsim 10\sigma$) than the observed luminosity reported in Table 1. In this work, we use MESA's default 'basic.net' nuclear reaction network as well as MESA's default settings for the equation of state (EOS) module. The EOS module uses a blend of different equation of state sources (including FreeEOS, OPAL/SCVH EOS, HELM, and SKYE EOS) to determine the thermodynamic properties of the models depending on the conditions of the stellar material (see A. S. Jermyn et al. 2023).

Model tracks are calculated incorporating diffusion of heavy elements following the prescription of A. A. Thoul et al. (1994), as well as a small amount of extra overshoot mixing beneath the convective envelope following an exponential profile with $f_{\rm ov,\,exp} = 0.01$ and $f_0 = 0.0005$. Envelope overshoot is applied following previous studies that found most models of low-mass red giant branch stars without envelope overshoot fail to reproduce the observed location of the red giant branch luminosity bump (M. Alongi et al. 1991; S. Khan et al. 2018; C. J. Lindsay et al. 2022). No extra overshoot mixing was incorporated above convective cores, since our stellar sample contains only low-mass stars, which do not have convective cores on the main sequence.

We model each star two different ways, changing only the treatment of metals. In the α-enhanced modeling, we use the same techniques that we apply in C. J. Lindsay et al. (2025), using element mixtures enhanced in α-elements from their GS98 values (N. Grevesse & A. J. Sauval 1998) according to the observed α abundances from Table 1. The α-enhanced models also are computed using correspondingly α-enhanced OPAL/Opacity Project opacity tables, included in MESA's kap module. For the Salaris-corrected stellar modeling, the MESA model element mixtures are scaled from the GS98 solar values, and the default non-α-enhanced GS98 opacity tables are used.

Along each evolutionary track, we save the global stellar model properties as well as the stellar structure files for models with luminosity, temperature, and [Fe/H] values that agree to within 10σ of the values in Table 1. We determine the cost function output based on the discrepancy between each stellar model and the target star observables, which is calculated as the sum of two χ^2 terms, one spectroscopic term and one asteroseismic term. The spectroscopic term, $\chi^2_{\rm spec}$, is determined as

$$\chi^2_{\rm spectroscopic} = \chi^2_{\rm Luminosity} + \chi^2_{\rm Temperature} + \chi^2_{\rm [Fe/H]} \tag{2}$$

with each spectroscopic parameter P's, corresponding χ^2_P value calculated as:

$$\chi^2_P = \frac{(P_{\rm obs} - P_{\rm model})^2}{\sigma^2_{P_{\rm obs}}}. \tag{3}$$

We find the [Fe/H] values for each α-enhanced model by taking the surface metal and hydrogen abundances from each MESA model, then calculating the iron abundance compared with the solar value (N. Grevesse & A. J. Sauval 1998), taking into account the different relative abundances of iron in the metal mixture given the alpha-enhancement values reported in Table 1. For the Salaris-corrected modeling, [Fe/H] is also found from the surface metal and hydrogen abundances, but since each model's metal abundances are solar-scaled, we can take [Fe/H] = [M/H] as there is no α-element enhancement.

In order to determine the fit to the observed asteroseismic data ($\chi^2_{\rm seismic}$), we calculate the radial, dipole, and quadrupole (ℓ = 0, 1, and 2) mode frequencies for models along the evolutionary tracks using the stellar oscillation code GYRE (R. H. D. Townsend & S. A. Teitler 2013). We first calculate the $\ell = 0$ mode frequencies for all models along the track with $\chi^2_{\rm spectroscopic} < 100$, then, for models with a close enough match ($\chi^2_{{\rm seismic},\ell=0} < 10$) between the observed and model $\ell = 0$ modes, we also calculate the $\ell = 1$ mixed modes and $\ell = 2$ p-modes. $\chi^2_{{\rm seismic},\ell=0}$ is found by finding the reduced χ^2 between the observed radial mode frequencies and the surface-corrected radial model frequencies using Equation 4.

We match each model p-mode ($\ell = 0, 2$) to the observed oscillation frequencies based on their inferred values of radial order ($n_{\rm p}$. The observed $n_{\rm p}$ values are based on the asymptotic relation ($n_{\rm p} \approx (\nu_{\rm obs}/\Delta\nu) - (\ell/2)$) and the observed $\Delta\nu$ values from Table 1, while the model mode $n_{\rm p}$ values are returned from the GYRE code. As more than one dipolar mixed mode can share the same $n_{\rm p}$ value, we match the model $\ell = 1$ modes to the observed modes using a nearest neighbor search. The $\ell = 0$ and $\ell = 2$ p-mode frequencies are corrected for known near-surface modeling errors (the 'surface term') using the two-term prescription from W. H. Ball & L. Gizon (2014). The $\ell = 0$ observed and model modes are used to determine the surface-term coefficients, which are then applied to the modes of other angular degrees. The $\ell = 1$ mixed mode frequencies are the result of mode coupling between a core g-mode component, which does not suffer a surface effect, and an envelope p-mode component, which does. Following J. M. J. Ong & S. Basu (2020) we apply the surface correction from W. H. Ball & L. Gizon (2014) to only the pure-p-mode (π-mode) component of the mixed-mode frequencies.

Subtracting the surface-corrected mode frequencies ($\nu_{{\rm corr\ model},n}$) from the observed frequencies ($\nu_{\rm obs}$), squaring this difference, and dividing by the squared observed mode frequency errors ($\sigma^2_{\nu_{{\rm obs},n}}$), we find the seismic χ^2 per degree of freedom, $\chi^2_{\rm seismic}$, for models along the evolutionary track using,

$$\chi^2_{\rm seismic} = \frac{1}{N_\nu - 1 - 2} \sum_n^{N_\nu} \frac{(\nu_{{\rm obs},n} - \nu_{{\rm corr\ model},n})^2}{\sigma^2_{\nu_{{\rm obs},n}}}, \tag{4}$$

where N_ν is the total number of mode frequencies. Since over-corrections in accounting for the surface term can make models whose mode frequencies are far from the observed frequencies seem like good model fits, we add an additional penalty function to $\chi^2_{\rm seismic}$ calculated from the 2 lowest frequency radial and quadrupole modes.

$$\chi^2_{{\rm low}\ n} = \frac{1}{100} \sum_{\ell\in\{0,2\}} \frac{1}{2} \sum_{n=0}^{1} \frac{(\nu_{{\rm obs},n} - \nu_{{\rm uncorr\ model},n})^2}{\sigma^2_{\nu_{{\rm obs},n}}}. \tag{5}$$

Similar terms of this type were also included in S. Basu & A. Kinnane (2018), J. M. J. Ong et al. (2021), M. S. Cunha et al. (2021), C. J. Lindsay et al. (2024), and C. J. Lindsay et al. (2025) ensuring that the lower frequency uncorrected model p-modes agree with the corresponding observed mode frequencies.

The sum of each model along the track's $\chi^2_{\rm spectroscopic}$, $\chi^2_{\rm seismic}$, and $\chi^2_{\rm low\ n}$ is the total χ^2 ($\chi^2_{\rm total}$) and the model with the minimum $\chi^2_{\rm total}$ is the best-fit model along the evolutionary track. That lowest $\chi^2_{\rm total}$ is returned by the cost function to the differential evolution optimization routine and is then used to choose subsequent combinations of initial model parameters. All $\chi^2_{\rm total}$ values along each track as well as the model parameters of each track's best-fit model are saved in order to determine the weighted distribution of the stellar parameter of interest. We calculate the weights of each model based on the $\chi^2_{\rm total}$ values by taking

$$W_{\rm model} = \frac{L_{\rm total}}{\sum L_{\rm total}}, \text{ with } L_{\rm total} = \frac{\exp(-\frac{1}{2}\frac{\chi^2_{\rm total}}{\chi^2_{\rm total,\ min}})}{p(M, Y_0, Z_0, \alpha_{\rm mlt})/dt} \quad (6)$$

where $p(M, Y_0, Z_0, \alpha_{\rm mlt})$ is the Kernel Density Estimation-based estimate of the local sampling density in mass, initial helium abundance, initial metallicity, and mixing length at that track's values of M, Y_0, Z_0, and $\alpha_{\rm mlt}$ and dt is the length of each stellar model's timestep. We note that when calculating the likelihoods, we first divide each $\chi^2_{\rm total}$ value by the minimum $\chi^2_{\rm total}$ along the entire optimization modeling run for that star. This is done because some stars, particularly those observed by *Kepler*, have very small mode frequency errors yielding some $\chi^2_{\rm total}$ that are orders of magnitude too large to calculate an associated L for without running into a floating-point underflow. Tempering all $\chi^2_{\rm total}$ values by the minimum $\chi^2_{\rm total}$ value reduces this problem for the *Kepler* stars.

We report the 16th, 50th, and 84th percentiles of the weighted mass, age, radius, initial helium abundance, convective mixing length, effective temperature, luminosity, and iron abundance distributions determined from the α-enhanced and Salaris-corrected modeling for each star in Table 2 and Table 3 respectively. Using the differential evolution algorithm ensures that the region of parameter space around the highest likelihood initial MESA model parameters is more densely sampled than if a grid with uniform sampling was applied, as in most other asteroseismic modeling studies. There is not a minimum $\chi^2_{\rm total}$ at which the optimization stops; instead, after 40 iterations of the differential evolution algorithm (corresponding to 840 cost function evaluations with each evaluation involving the calculation of the MESA evolutionary track, model mode frequencies, and determining the best-fit model and associated $\chi^2_{\rm total}$), the best fit model among all models from all model tracks is taken as the overall best-fit model. The parameters of the best-fit models resulting from the separate α-enhanced and Salaris-corrected modeling procedures are reported in Table 4 and Table 5 respectively.

We visualize the resultant weighted parameter distributions from the α-enhanced and Salaris-corrected modeling procedure applied to the final target star in our sample, TIC 300085386, in Figure 3 and Figure 4. The corner plots in Figure 3 and Figure 4 are constructed by taking the parameters of the best fit (lowest $\chi^2_{\rm total}$) models along each track calculated as part of the α-enhanced and Salaris-corrected optimization procedures, weighted according to Equation 6. The marginal distribution plots along the diagonal in Figure 3 show the mass, radius, and age distributions in the form of kernel density estimation (KDE) plots for all the α-enhanced models in blue and the Salaris-corrected models in red. Similarly, the marginal distribution plots in Figure 4 show the [Fe/H], effective temperature, and luminosity distributions for the same set of α-enhanced and Salaris-corrected models.

In each marginal distribution plot in Figure 3 and Figure 4, the blue and red solid vertical lines show the 50th percentiles of the likelihood-weighted parameter distributions from the α-enhanced and Salaris-corrected modeling, respectively, while the blue and red shaded regions span the region between the 16th and 84th percentiles of the same weighted parameter distributions. The vertical dashed blue and red lines in the marginal distribution plots of Figure 3 and Figure 4 show the α-enhanced and Salaris-corrected best-fit model parameters, respectively. The vertical dot-dashed black lines in Figure 4 show the observed values for luminosity, effective temperature, and [Fe/H], with the Salaris-corrected [Fe/H] value shown with an orange vertical dashed line.

The blue and red contours in the off-diagonal panels of Figure 3 and Figure 4 show the joint distributions between parameter pairs along with data points showing the best-fit model parameters and associated errors from the α-enhanced modeling (Table 4, blue circle points) and the Salaris-corrected modeling (Table 5, red star points). The observed spectroscopic parameters listed in Table 1 for HD 128279 are represented as gray 2σ error ellipses in the joint distribution plots in Figure 4. The orange 2σ error ellipses show the Salaris-corrected [Fe/H] observations. Equivalent corner plots for the other stars in our sample are shown in Appendix C.

4. RESULTS

We report the global parameters of the stars in our sample, derived using α-enhanced models, in Table 2. The quoted upper and lower uncertainties correspond to the differences between the 84th and 50th percentiles and between the 50th and 16th percentiles, respectively. Similarly, Table 3 reports

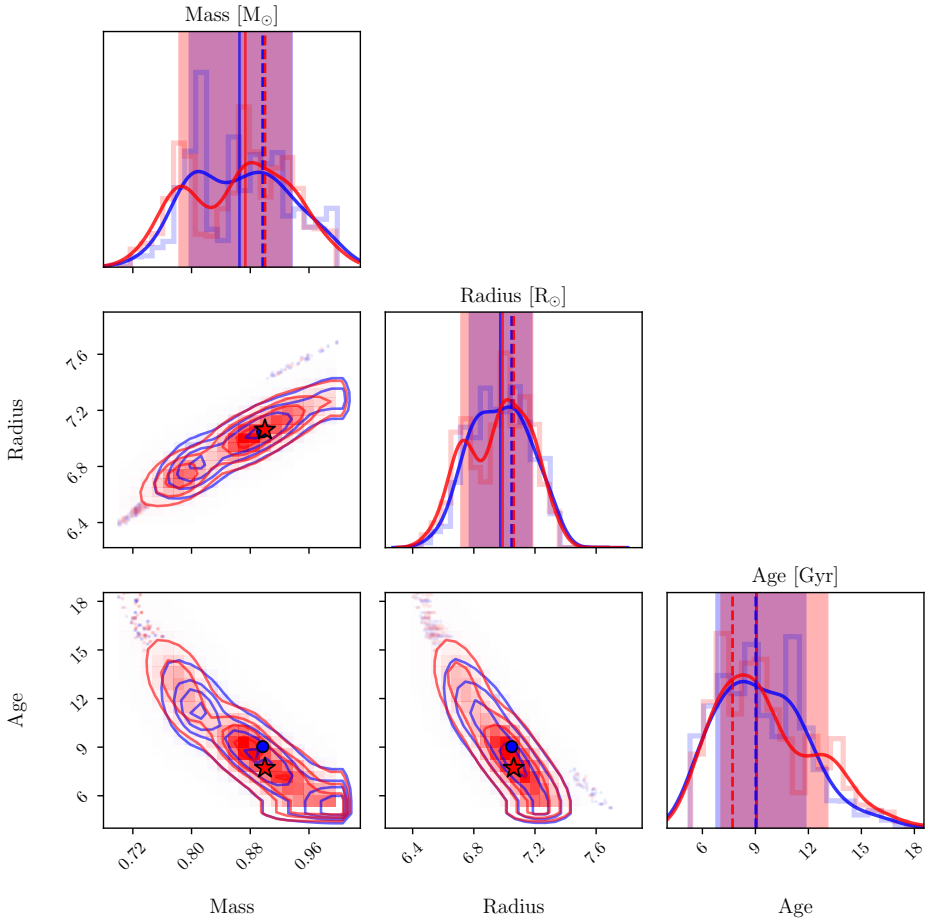

Figure 3. Corner plot visualization showing the mass, radius, and age results of the α-enhanced and Salaris-corrected modeling procedure applied to TIC 300085386. The model parameters are taken from the best-fit model from each evolutionary track, and the parameters are weighted by the normalized likelihood (Equation 6) before plotting. The on-diagonal panels show the marginal mass, radius, and age distributions in the form of kernel density estimation (KDE) plots with blue curves showing the α-enhanced results and red curves showing the Salaris-corrected results. The vertical blue and red lines over-plotted in the on-diagonal panels show the 50th percentiles of the likelihood-weighted parameter distributions from the α-enhanced and Salaris-corrected modeling, respectively, while the blue and red shaded regions span the region between the 16th and 84th percentiles of the same weighted parameter distributions. The vertical blue and red dashed lines show the best-fit α-enhanced and Salaris-corrected model parameters, respectively. The blue and red contours in the off-diagonal panels show the joint distributions of different pairs of global stellar parameters derived from the α-enhanced and Salaris-corrected modeling procedures, respectively. The data points in the off-diagonal plots show the overall best-fit model parameters from the α-enhanced modeling (blue circle points) and the Salaris-corrected modeling (red star points) of TIC 300085386.

the global parameter results for our sample of stars derived using Salaris-corrected models.

We find that the global parameters of the stars in our sample obtained using our α-enhanced modeling procedure agree well with the parameters obtained by applying the correction of M. Salaris et al. (1993) to the observed [Fe/H] values and running the same asteroseismic modeling procedure using non-α-enhanced (solar-scaled) stellar models. We illustrate this finding using 'one-to-one' plots for the inferred masses (Figure 5), radii (Figure 6), and ages (Figure 7). Each 'one-to-one' plot displays the mass, radius, or age results derived from the α-enhanced modeling on the x-axis and the corresponding mass, radius, or age results from Salaris-corrected modeling on the y-axis, along with the associated asymmetric errors on the stellar parameters.

Each star's α-enhanced and Salaris-corrected mass result shown in Figure 5 agree with each other at the 1σ level, meaning all points in the 'one-to-one' plot lie along the dashed line of equality when mass errors are taken into account. Similarly, Figure 6 shows that all the α-enhanced and Salaris-corrected radii results agree to within 1σ. Finally, the α-enhanced and Salaris-corrected age results shown in Figure 7 show that the age determinations also agree between methods of accounting for α-enhancement for all stars in our sample to within 1σ. Overall, these results show that when using asteroseismic data, both modeling methods for

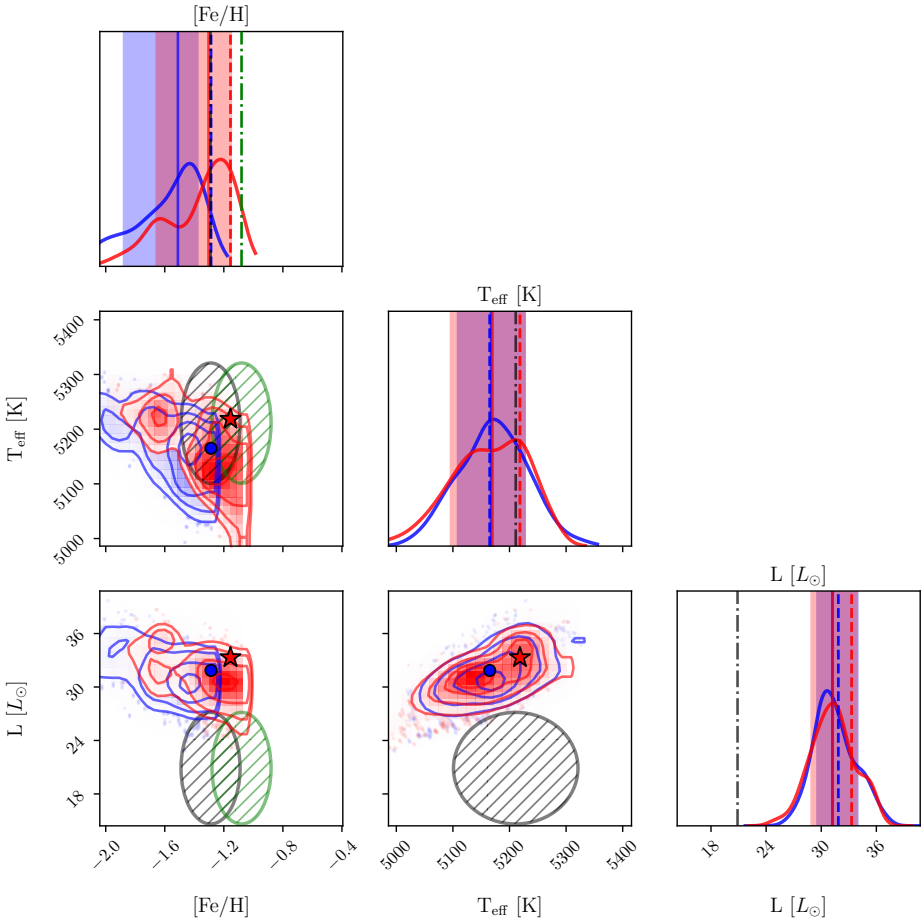

Figure 4. Similar corner plot to Figure 3 except we show the [Fe/H], T_{eff}, and luminosity distributions from the α-enhanced and Salaris-corrected modeling procedure applied to TIC 300085386. The vertical black dot-dashed lines in each on-diagonal panel show the observed [Fe/H], T_{eff}, and luminosity values, with the Salaris-corrected [Fe/H] value shown with a red vertical dot-dashed line. The spectroscopic observations are represented in the off-diagonal joint-distribution panels as 2σ gray ellipses. The orange 2σ ellipses incorporate the Salaris correction to the observed [Fe/H].

Table 2. Asteroseismic modeling results for all target stars using the α-enhanced modeling method. Each parameter value and range represents the 16th, 50th, and 84th percentiles calculated from the parameters weighted by the normalized likelihood (Equation 6).

Target	Mass [$M_\odot$]	Age [Gyr]	Radius [$R_\odot$]	Y_0	α_{mlt}	T_{eff} [K]	L [$L_\odot$]	[Fe/H]	$\Delta\Pi_{\ell=1}$ [s]
HD 128279	$0.808^{+0.036}_{-0.050}$	$10.7^{+2.7}_{-1.6}$	$3.761^{+0.107}_{-0.047}$	$0.256^{+0.006}_{-0.009}$	$1.76^{+0.12}_{-0.12}$	5397^{+34}_{-30}	$10.95^{+0.33}_{-0.32}$	$-2.16^{+0.04}_{-0.04}$	$86.06^{+1.02}_{-2.65}$
HD 140283	$0.768^{+0.038}_{-0.026}$	$12.5^{+1.7}_{-1.8}$	$2.103^{+0.075}_{-0.057}$	$0.258^{+0.010}_{-0.008}$	$1.80^{+0.17}_{-0.15}$	5807^{+56}_{-54}	$4.54^{+0.30}_{-0.29}$	$-2.24^{+0.23}_{-0.16}$	$146.45^{+9.85}_{-1.30}$
HD 175305	$0.795^{+0.027}_{-0.021}$	$12.3^{+2.1}_{-1.3}$	$7.309^{+0.080}_{-0.078}$	$0.259^{+0.009}_{-0.011}$	$1.83^{+0.11}_{-0.16}$	5084^{+83}_{-47}	$32.44^{+2.41}_{-1.92}$	$-1.34^{+0.20}_{-0.34}$	$64.92^{+0.50}_{-0.66}$
KIC 4671239	$0.758^{+0.062}_{-0.036}$	$14.1^{+2.8}_{-3.6}$	$5.172^{+0.157}_{-0.099}$	$0.255^{+0.011}_{-0.008}$	$1.80^{+0.14}_{-0.14}$	5262^{+76}_{-81}	$18.48^{+1.88}_{-1.45}$	$-1.62^{+0.34}_{-0.52}$	$72.03^{+1.05}_{-1.06}$
KIC 7341231	$0.781^{+0.036}_{-0.031}$	$12.9^{+1.4}_{-1.4}$	$2.562^{+0.047}_{-0.044}$	$0.258^{+0.009}_{-0.008}$	$1.74^{+0.13}_{-0.11}$	5419^{+73}_{-82}	$5.13^{+0.30}_{-0.39}$	$-1.46^{+0.10}_{-0.19}$	$111.68^{+0.06}_{-0.14}$
KIC 8144907	$0.737^{+0.023}_{-0.017}$	$14.6^{+1.5}_{-1.3}$	$3.516^{+0.032}_{-0.036}$	$0.261^{+0.006}_{-0.011}$	$1.86^{+0.11}_{-0.18}$	5454^{+31}_{-63}	$9.83^{+0.39}_{-0.53}$	$-2.61^{+0.22}_{-0.25}$	$84.69^{+0.22}_{-0.22}$
ν Indi	$0.797^{+0.039}_{-0.019}$	$12.1^{+1.3}_{-1.5}$	$2.812^{+0.041}_{-0.029}$	$0.255^{+0.010}_{-0.007}$	$1.87^{+0.16}_{-0.12}$	5409^{+85}_{-61}	$6.14^{+0.43}_{-0.42}$	$-1.49^{+0.06}_{-0.05}$	$102.98^{+0.06}_{-0.08}$
TIC 300085386	$0.875^{+0.062}_{-0.083}$	$8.8^{+3.1}_{-2.0}$	$6.996^{+0.179}_{-0.229}$	$0.258^{+0.008}_{-0.009}$	$1.77^{+0.15}_{-0.13}$	5168^{+62}_{-64}	$31.31^{+2.62}_{-2.13}$	$-1.51^{+0.14}_{-0.38}$	$66.57^{+0.47}_{-0.55}$

accounting for α-enhancement, Salaris-corrected or fully α-enhanced, produce very similar mass, radius, and age posterior results.

The average precision on our different stellar parameter results is ~4% in mass, ~2% in radius, and ~15% in age. These levels of precision on mass, radius, and age are generally in line with previous asteroseismic studies of main se-

Table 3. Asteroseismic modeling results for all target stars using the Salaris-corrected modeling method. Each parameter value and range represents the 16th, 50th, and 84th percentiles calculated from the parameters weighted by the normalized likelihood (Equation 6).

Target	Mass [$M_\odot$]	Age [Gyr]	Radius [$R_\odot$]	Y_0	α_{mlt}	T_{eff} [K]	L [$L_\odot$]	[Fe/H]	$\Delta\Pi_{\ell=1}$ [s]
HD 128279	$0.796^{+0.042}_{-0.044}$	$11.2^{+2.6}_{-1.4}$	$3.763^{+0.067}_{-0.067}$	$0.252^{+0.010}_{-0.006}$	$1.83^{+0.07}_{-0.12}$	5417^{+33}_{-35}	$10.90^{+0.40}_{-0.27}$	$-1.93^{+0.03}_{-0.04}$	$85.03^{+2.08}_{-1.69}$
HD 140283	$0.776^{+0.032}_{-0.032}$	$12.1^{+1.9}_{-1.3}$	$2.107^{+0.065}_{-0.062}$	$0.259^{+0.006}_{-0.008}$	$1.79^{+0.15}_{-0.16}$	5818^{+59}_{-62}	$4.58^{+0.32}_{-0.32}$	$-1.92^{+0.19}_{-0.16}$	$148.35^{+9.26}_{-2.59}$
HD 175305	$0.790^{+0.035}_{-0.018}$	$12.7^{+1.6}_{-2.0}$	$7.294^{+0.093}_{-0.063}$	$0.259^{+0.009}_{-0.011}$	$1.78^{+0.17}_{-0.13}$	5106^{+73}_{-93}	$32.58^{+2.31}_{-2.83}$	$-1.22^{+0.21}_{-0.32}$	$64.49^{+0.78}_{-0.41}$
KIC 4671239	$0.746^{+0.074}_{-0.030}$	$14.8^{+2.4}_{-4.6}$	$5.147^{+0.176}_{-0.082}$	$0.257^{+0.010}_{-0.009}$	$1.81^{+0.13}_{-0.14}$	5268^{+74}_{-78}	$18.58^{+1.78}_{-1.70}$	$-1.58^{+0.37}_{-0.77}$	$71.55^{+0.95}_{-0.69}$
KIC 7341231	$0.783^{+0.035}_{-0.034}$	$12.7^{+1.6}_{-1.4}$	$2.569^{+0.039}_{-0.049}$	$0.258^{+0.008}_{-0.008}$	$1.74^{+0.17}_{-0.10}$	5427^{+74}_{-64}	$5.14^{+0.38}_{-0.31}$	$-1.29^{+0.15}_{-0.20}$	$111.64^{+0.08}_{-0.05}$
KIC 8144907	$0.752^{+0.026}_{-0.031}$	$13.9^{+1.9}_{-1.4}$	$3.538^{+0.048}_{-0.044}$	$0.253^{+0.009}_{-0.005}$	$1.85^{+0.14}_{-0.13}$	5433^{+76}_{-53}	$9.86^{+0.76}_{-0.50}$	$-2.31^{+0.23}_{-0.23}$	$84.79^{+0.26}_{-0.19}$
ν Indi	$0.801^{+0.037}_{-0.022}$	$12.2^{+1.1}_{-2.1}$	$2.817^{+0.040}_{-0.034}$	$0.256^{+0.009}_{-0.008}$	$1.88^{+0.22}_{-0.11}$	5413^{+95}_{-70}	$6.11^{+0.70}_{-0.38}$	$-1.17^{+0.04}_{-0.04}$	$102.91^{+0.10}_{-0.07}$
TIC 300085386	$0.866^{+0.061}_{-0.089}$	$9.3^{+3.8}_{-2.2}$	$6.970^{+0.189}_{-0.261}$	$0.258^{+0.008}_{-0.009}$	$1.77^{+0.14}_{-0.12}$	5165^{+61}_{-77}	$30.81^{+2.48}_{-2.56}$	$-1.28^{+0.14}_{-0.37}$	$66.55^{+0.44}_{-0.60}$

quence stars (e.g. E. P. Bellinger et al. 2019) as well as more evolved stars (e.g. C. J. Lindsay et al. 2024). An inspection of the KDE plots and joint distribution plots in Figure 3 shows that weighted distributions in mass, radius, and age calculated based on the lowest $\chi^2_{\rm total}$ Salaris-corrected models from each evolutionary track are significantly more multimodal compared with the distribution of parameters resulting from the α-enhanced modeling. This trend is also visible by inspection of the corner plots for the other target stars in Appendix C. Overall, these wider and typically more strongly bimodal distributions in mass, radius, and age resulting from the Salaris-corrected modeling result in consistently larger uncertainties in the inferred parameters when performing asteroseismic modeling using the Salaris correction, though this effect is small. Taking the average of the upper and lower errors for each target star and then averaging the parameter errors for all target stars analyzed with a given modeling method, the mean percent error in mass across the 8 stars in our sample is about 5% when using the Salaris correction and about 4% when using the full α-enhancement treatment. Consequently, the average percent error in age is higher (~17%) for the Salaris-corrected modeling compared with ~15% age errors when applying the α-enhanced modeling methods. The average percent error in radius is approximately constant (2%) for both the Salaris-corrected modeling and α-enhanced modeling.

4.1. *Best-fit Models*

We also report the global parameters of the best-fit α-enhanced models for each target star in Table 4 and the parameters of the best-fit Salaris-corrected models in Table 5. The individual best-fit model masses, radii, and ages are visualized with the vertical dashed lines in the on-diagonal panels of the global parameter corner plots (Figure 3 and left-hand plots of the figures in Appendix C) and with the circle and star points in the off-diagonal joint distribution panels in the global parameter corner plots. The best-fit masses, radii, and ages generally coincide with the dense regions of each parameter's likelihood-weighted distribution, with the

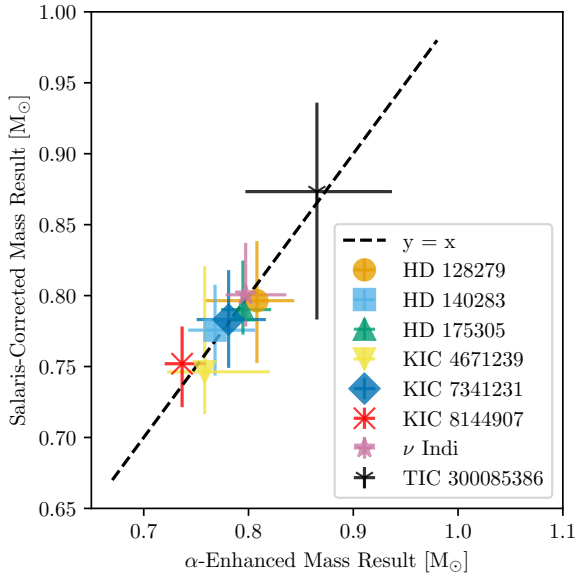

Figure 5. The α-enhanced and Salaris-corrected stellar mass modeling results are shown in a 'one-to-one' plot. The dashed black line shows the line of equality. Both modeling methods produce masses that agree with each other to within ~ 1σ, indicating that the method for accounting for α-enhancement does not significantly change the inferred stellar mass.

vertical dashed lines agreeing with the shaded areas representing the area between the 16th and 84th percentiles of the likelihood-weighted parameter distributions. We show the best-fit model [Fe/H], effective temperature, and luminosity parameters as vertical dashed lines and data points in the spectroscopic quantity corner plots (Figure 4 and right-hand plots of the figures in Appendix C.) As is apparent in Figure 4, the best-fit model's spectroscopic parameters do not always agree exactly with the observed spectroscopic properties. In the case of TIC 300085386, Figure 4 shows that the observed luminosity is substantially lower than the best-fit model luminosities obtained from both our α-enhanced and Salaris-corrected asteroseismic modeling. Mismatches

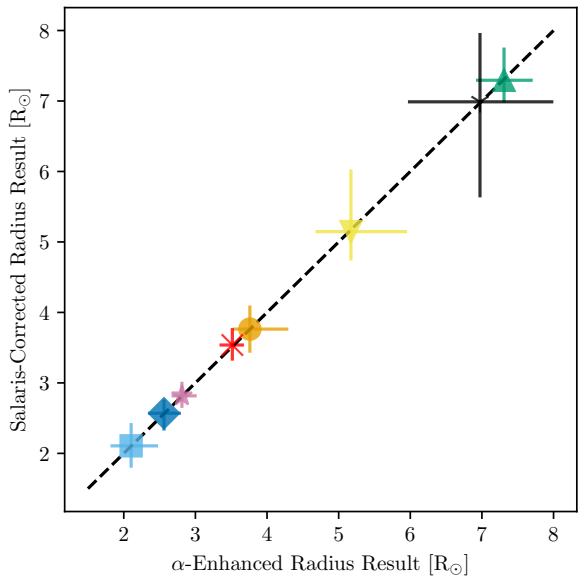

Figure 6. Same as Figure 5 except the modeling results for stellar radii are shown, with error bars expanded by 5 times to allow them to be visible.

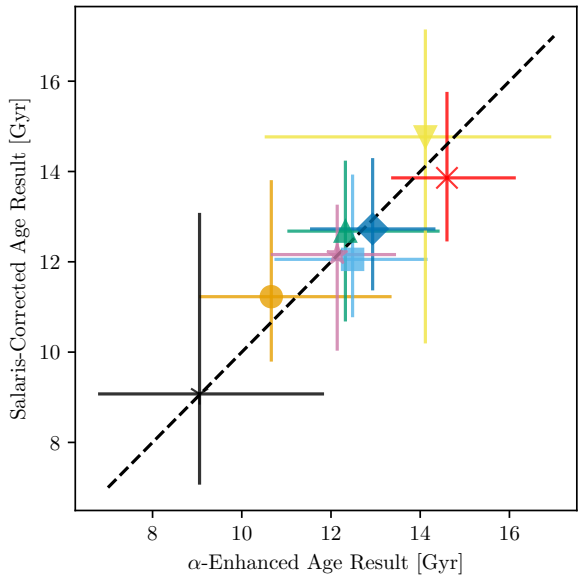

Figure 7. Same as Figure 5 except the modeling results for stellar age are shown.

between the observed spectroscopic parameters and the asteroseismic modeling-based spectroscopic parameters could indicate that the observations are inaccurate; for example, the luminosity of TIC 300085386 is obtained using only GAIA photometry, which is known to give inaccurate luminosities due to a variety of factors, including imperfect dust extinction corrections (Gaia Collaboration et al. 2018).

The best-fit masses we determine for the stars in our sample are generally quite low, ranging between about 7.5 and 0.9 $M_\odot$. Thus, the best-fit ages we infer are hence quite old, with all stars except TIC 300085386 having ages between about 11 and 14 Gyr. Since the early enrichment of the Galaxy is thought to be dominated by more core-collapse supernovae, which produce higher concentrations of α elements compared with later type 1a supernovae, the fact that we infer old ages for our target stars is in line with the fact that all the target stars in our sample are evolved, metal-poor, and enhanced in α-elements.

We note that as in C. J. Lindsay et al. (2025), the age of the universe ($\tau_{\rm universe} \simeq 13.8$ Gyr (Planck Collaboration et al. 2020)) was not explicitly used as a stopping condition in our MESA modeling; however, there is an effective age cutoff enforced through our adopted stellar mass lower bound of $0.7 M_\odot$. However, since many stellar models with $M \lesssim 0.77 {\rm M}_\odot$ are older than $\tau_{\rm universe}$ at the metallicities and evolutionary stages under consideration in this work, it is possible for a target star's best fit model to be older than the universe. This only occurred for the α-enhanced best-fit model for HD 128279; however, we find that the age of HD 128279 is not in tension with the age of the universe when the width of the weighted distribution of ages is taken into account. The lower right panel of Figure 3 shows the best-fit model age for HD 128279 is far on the higher age end of the age distribution, and the 50th percentile of the weighted age distribution is at 12 Gyr, less than the age of the universe.

The α-enhanced and Salaris-corrected best-fit ages for the youngest star in our sample, TIC 300085386, are approximately 1.3 Gyr apart, with the α-enhanced stellar model being older. This age difference is slightly more than the error in age we estimate by examination of the likelihood-weighted age distributions determined for TIC 300085386. Inspecting the model parameters of the best-fit Salaris-corrected model for TIC 300085386, the initial helium abundance ($Y_0 = 0.268$) is near solar and higher than expected for a metal-poor star, which has presumably not been enhanced much beyond the primordial helium abundance. This may be the reason for the large discrepancy in age between α-enhanced and Salaris-corrected best-fit models.

4.2. *Dipolar Gravity Mode Period Spacings*

A star's asymptotic gravity mode period spacing ($\Delta\Pi_\ell$) refers to the spacing between consecutive g-modes of high radial order (n) and the same spherical degree, ℓ. $\Delta\Pi_\ell$ is sensitive to the size and buoyancy frequency profile of the stellar core and is calculated from stellar models as

$$\Delta\Pi_\ell = \frac{2\pi^2}{\sqrt{\ell(\ell+1)}} \left(\int_{\rm core} \frac{N}{r} dr \right)^{-1} \tag{7}$$

where ℓ is the angular degree, r is the radius coordinate, N is the Brunt–Väisälä frequency, and the integral is taken over

Table 4. The global parameters of the individual best-fit α-enhanced models for each target star along the optimization trajectory.

Target	Mass [$M_\odot$]	Age [Gyr]	Radius [$R_\odot$]	Y_0	α_{mlt}	T_{eff} [K]	Luminosity [$L_\odot$]	[Fe/H]
HD 128279	0.764	14.1	3.788	0.245	1.95	5432	11.26	−2.17
HD 140283	0.763	13.0	2.094	0.256	1.85	5818	4.52	−2.31
HD 175305	0.812	11.3	7.340	0.261	1.96	5186	35.12	−1.38
KIC 4671239	0.808	11.2	5.323	0.249	1.73	5311	20.31	−2.69
KIC 7341231	0.782	13.2	2.567	0.258	1.65	5327	4.78	−1.34
KIC 8144907	0.756	13.6	3.547	0.257	1.98	5469	10.14	−2.20
ν Indi	0.796	12.7	2.804	0.254	1.82	5370	5.89	−1.45
TIC 300085386	0.897	9.0	7.048	0.247	1.92	5165	31.85	−1.29

Table 5. The global parameters of the individual best-fit Salaris-corrected models for each target star along the optimization trajectory described in section 3.

Target	Mass [$M_\odot$]	Age [Gyr]	Radius [$R_\odot$]	Y_0	α_{mlt}	T_{eff} [K]	Luminosity [$L_\odot$]	[Fe/H]
HD 128279	0.774	13.2	3.809	0.247	1.92	5431	11.38	−2.02
HD 140283	0.747	13.1	2.075	0.266	1.96	5909	4.73	−2.30
HD 175305	0.822	11.5	7.371	0.252	1.80	5101	33.14	−1.21
KIC 4671239	0.794	11.6	5.278	0.256	1.73	5279	19.48	−1.87
KIC 7341231	0.781	12.7	2.569	0.264	1.71	5368	4.94	−1.17
KIC 8144907	0.770	13.1	3.569	0.252	1.99	5475	10.31	−2.01
ν Indi	0.795	12.9	2.803	0.254	1.79	5343	5.77	−1.13
TIC 300085386	0.900	7.7	7.061	0.268	1.93	5218	33.31	−1.16

the extent of the radiative core of a star (M. Tassoul 1980). To test if applying different treatments of α-enhancement changes the inferred model asymptotic dipolar period spacing, we applied Equation 7 to the models we calculate in our modeling procedure to determine posterior distributions of $\Delta\Pi_{\ell=1}$ resulting from the α-enhanced and Salaris-corrected modeling of the stars in our sample. We report the posterior predictive $\Delta\Pi_{\ell=1}$ results for our α-enhanced and Salaris-corrected modeling in the last columns of Table 2 and Table 3 respectively. Overall, we find that the $\Delta\Pi_{\ell=1}$ results from both modeling methods agree closely (within the 1σ level for all stars in the sample), meaning the α-enhanced and Salaris-corrected stellar models, which match the observed stellar properties, have similar core properties.

We note that the 1σ errors on $\Delta\Pi_{\ell=1}$ we derive from our modeling are all larger than the uncertainties on $\Delta\Pi_{\ell=1}$, which are typically obtained from analysis of *Kepler* data — in some cases considerably so. Observed errors on $\Delta\Pi_{\ell=1}$ can be very small given the high quality of data available. For example, D. Huber et al. (2024) and J. S. Kuszlewicz et al. (2023) found $\Delta\Pi_{\ell=1} = 84.83 \pm 0.02$ s by modeling the power spectrum of KIC 8144907. In our α-enhanced and Salaris-corrected modeling of KIC 8144907, we find $\Delta\Pi_{\ell=1} = 84.69^{+0.22}_{-0.22}$ s and $\Delta\Pi_{\ell=1} = 84.79^{+0.26}_{-0.19}$ s, respectively, in 1σ agreement with the $\Delta\Pi_{\ell=1}$ measurement from D. Huber et al. (2024) but with much larger posterior uncertainties.

The large $\Delta\Pi_{\ell=1}$ uncertainties we report arise due to incompleteness in the observed set of dipolar mixed modes, in combination with the use of a nearest-neighbor matching scheme to compare the observed and model dipolar mode frequencies. Since only the most p-mode-dominated dipolar mixed-mode frequencies are observable, we are not able to match every model mixed mode to a corresponding observed mode. This means potentially erroneous matches between mixed modes of different g-mode radial order (n_g) — such as might occur where one more or one less model mixed mode exists in intervals where the dipole modes of the true star are not observable — may still result in low $\chi^2_{\rm seismic}$ values being computed from nearest-neighbor frequency matching. Therefore, models with significantly different values of $\Delta\Pi_{\ell=1}$ from the true star may still have mode frequencies within the observable ranges that closely match the observed ones. This is of particular concern in the case of HD 140283, where the TESS data yield only a very small number of dipolar mixed modes. Thus, the posteriors we obtain for $\Delta\Pi_{\ell=1}$ are wide since they are made from models where the computed mixed modes may be of entirely different identities than those in the true star but are assigned high likelihoods all the same.

5. DISCUSSION

5.1. *Asteroseismic Scaling Relations versus Individual Frequency Modeling*

Our results qualitatively disagree with those of L. M. Morales et al. (2025), who find that stellar ages inferred from 1D stellar-evolution models depend strongly on modelling assumptions — including, in particular, opacity tables and chemical mixtures, both of which are varied in this work. One possible reason for discrepancy is that, while asteroseismic constraints in L. M. Morales et al. (2025) were provided only by $\Delta\nu$ and $\nu_{\rm max}$, and then only through scaling relations, those in this work did not rely on scaling relations at all — our models were constrained instead only by numerical frequencies of oscillation, and without $\nu_{\rm max}$.

Previous works that used individual mode frequencies to determine the global parameters of metal-poor stars have found that the results obtained by using only the global asteroseismic parameters ($\Delta\nu$ and $\nu_{\rm max}$) disagree significantly with results obtained using individual mode frequencies (e.g. D. Huber et al. 2024; J. R. Larsen et al. 2025; C. J. Lindsay et al. 2025, and Lundkvist et al. (submitted)). In particular, scaling relation-based masses for metal-poor stars are significantly higher than masses obtained using detailed frequency modeling. Other works focused on applying the global asteroseismic scaling relations to stars in the Milky Way's Halo have also found that global asteroseismology gives stellar mass results that are larger than expected for old, metal-poor Halo stars (e.g. C. R. Epstein et al. 2014), highlighting the need for detailed asteroseismology when analyzing metal-poor stars.

Recent work examining the ramifications of surface effects on the asteroseismic scaling relation for $\Delta\nu$ ($\Delta\nu \propto \sqrt{\rho}$, T. M. Brown et al. 1991) has found that the systematic offsets in $\Delta\nu$ resulting from near-surface modeling errors are not able to fully account for the large variations between the results from global seismology and individual frequency modeling (T. Li et al. 2022; Y. Li et al. 2023; D. Huber et al. 2024). This indicates that the scaling relation for $\nu_{\rm max}$ $\nu_{\rm max}$ ($\nu_{\rm max} \propto g\mathrm{T}_{\rm eff}^{-1/2}$, H. Kjeldsen & T. R. Bedding 1995) fails at low metallicities. In this work, we use the same method to determine the global parameters for 8 metal-poor targets with individual mode frequencies, permitting a homogeneous determination of how the measured $\nu_{\rm max}$ values differ from the $\nu_{\rm max}$ values implied by the inferred mass, radius, and effective temperature results listed in Table 2 and Table 3. We quantify this deviation following S. Sharma et al. (2016); Y. Li et al. (2024); D. Huber et al. (2024); J. R. Larsen et al. (2025); C. J. Lindsay et al. (2025) calculating $f_{\nu_{\rm max}}$ using the following equation

$$f_{\nu_{\rm max}} = \frac{\nu_{\rm max}}{\nu_{\rm max,\odot}}\left(\frac{M}{\mathrm{M}_\odot}\right)^{-1}\left(\frac{R}{\mathrm{R}_\odot}\right)^{2}\left(\frac{T_{\rm eff}}{\mathrm{T}_{\rm eff,\odot}}\right)^{1/2}. \quad (8)$$

We plug in the mass, radius, and temperature of each best-fit model along every evolutionary track calculated as part of the α-enhanced or Salaris-corrected modeling procedure. Then we determine the likelihood weighted distribution of $f_{\nu_{\rm max}}$ in the same way we find the weighted distributions of the other parameters, determining the 16th, 50th, and 84th percentiles. We show the $f_{\nu_{\rm max}}$ percentile results for our sample of stars in Figure 8 with each panel showing the $f_{\nu_{\rm max}}$ results as a function of the observed [Fe/H]. The left and right panels of Figure 8 show the $f_{\nu_{\rm max}}$ results derived from our α-enhanced and Salaris-corrected modeling procedure, respectively. Since our mass, radius, and temperature results derived from using α-enhanced and Salaris-corrected stellar models are largely similar, the panels of Figure 8 are largely the same; however, the errors in $f_{\nu_{\rm max}}$ are generally larger in the Salaris-corrected due to the larger parameter errors obtained in our Salaris-corrected modeling.

The results shown in Figure 8 show that our modeling corroborates the findings of D. Huber et al. (2024), J. R. Larsen et al. (2025), and Lundkvist et al. (submitted), which all found for the metal-poor stars they modeled that the observed $\nu_{\rm max}$ values were larger than the $\nu_{\rm max}$ values obtained by imputing the masses, radii, and temperatures they derived using individual frequency modeling into the $\nu_{\rm max}$ scaling relation, resulting in similar positive values of $f_{\nu_{\rm max}}$.

5.2. *Comparison with the Original Modeling Works for the Stars in our Sample*

The goal of this work was to perform a homogeneous modeling of 8 metal-poor stars with two different methods of accounting for enhancement in α-elements. We performed our own modeling for each of the stars. However, since 7 of the 8 stars were previously studied using detailed asteroseismology, we compare our results with those previous works in this section and broadly find that despite differences in modeling methods, our results agree with the various previous asteroseismic analyses of these stars.

5.2.1. *HD 175305 and HD 128279*

Although the modeling procedure used to determine the parameters of HD 175305 and HD 128279 in C. J. Lindsay et al. (2025) was largely the same as the α-enhanced modeling method carried out in this work (section 3), we re-ran the α-enhanced modeling for this study since there were slight differences in the allowed optimizer parameter ranges used in this work, and, in this work, we report the medians and $\pm1\sigma$ uncertainties for the likelihood-weighted parameter distributions in addition to the parameters of the overall best-fit model parameters. For HD 128279, we find that the mass ($0.808^{+0.036}_{-0.050}M_\odot$) and radius ($3.761^{+0.107}_{-0.047}R_\odot$) results we determined using the α-enhanced modeling method in this work agree to 1σ with the results from C. J. Lindsay et al. (2025) ($M = 0.77 \pm 0.02 M_\odot$, $R = 3.80 \pm 0.03 R_\odot$). The corresponding

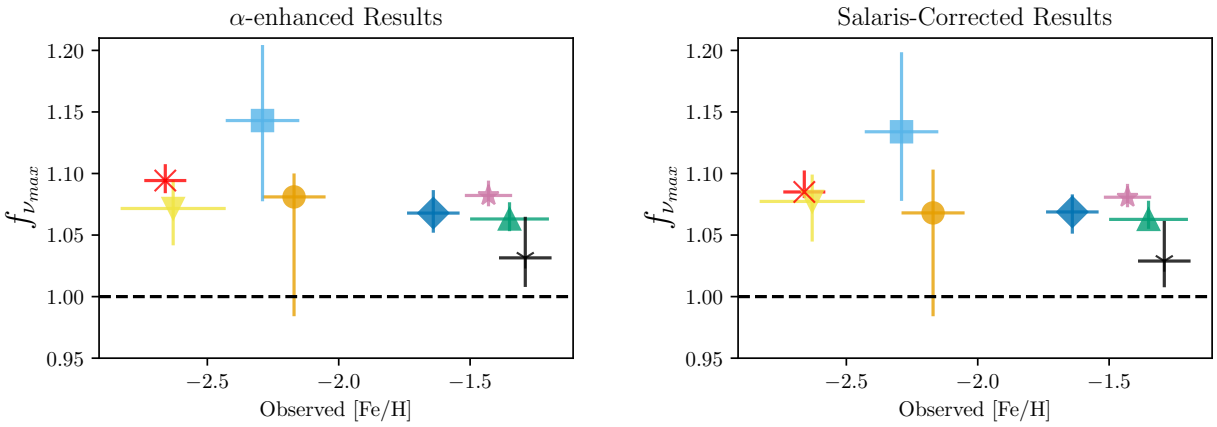

Figure 8. The $f_{\nu_{\rm max}}$ results inferred using our α-enhanced modeling results (left) and Salaris-corrected results (right). The error bars represent the modeling [Fe/H] errors on the x-axis and the 16th to 84th percentile calculated from the weighted $f_{\nu_{\rm max}}$ distributions for each star. See the legend of Figure 5 to see which symbol corresponds to which star.

age determined in C. J. Lindsay et al. (2025) (12.5 ± 1 Gyr) is also consistent with the age we determine using α-enhanced models in this work ($10.07^{+2.7}_{-1.6}$ Gyr), with agreement at the 1σ level.

For HD 175305, we find that the mass ($0.795^{+0.027}_{-0.021}$ $M_\odot$) and radius ($7.309^{+0.080}_{-0.078}$ $R_\odot$) we determined using the α-enhanced modeling method in this work agree to 1σ with the HD 175305 results from C. J. Lindsay et al. (2025) ($M = 0.83 \pm 0.02 M_\odot$, $R = 7.4 \pm 0.07 R_\odot$). The ages determined for HD 175305 in both C. J. Lindsay et al. (2025) (11.16 ± 0.91 Gyr) and this work ($12.3^{+2.1}_{-1.3}$ Gyr) are also in close 1σ agreement.

Since the weighted mass, radius, and age parameter distributions calculated based on the Salaris-corrected models for HD 128279 and HD 175305 agree closely with the distributions from the α-enhanced modeling (see Figure 5, Figure 6, Figure 7), the results from C. J. Lindsay et al. (2025) also agree closely with our Salaris-corrected mass, radius, and age modeling results.

5.2.2. *HD 140283*

Lundkvist et al. (submitted) performed individual frequency modeling of HD 140283, also known as the Methuselah star, using a dense grid of models. They find a mass of 0.75 ± 0.01, a radius of $2.075^{+0.011}_{-0.012}$, and an age of 14.4 ± 0.4 Gyr for HD 140283. Based on their results, they also calculate an $f_{\nu_{\rm max}}$ value of 1.14 ± 0.03 based on their modeling. There is good agreement between the BASTA (V. Silva Aguirre et al. 2015) modeling carried out in Lundkvist et al. (submitted) and this work, which is expected since, although we use a MESA/GYRE-based approach, the mode frequencies and spectroscopic inputs are the same. The mass, age, and radius values we determine for HD 140283 using both the α-enhanced and Salaris-corrected modeling methods agree within 1σ with the results from Lundkvist et al. (submitted). As our global properties are similar, the $f_{\nu_{\rm max}}$ we determine for HD 140283 (~1.14 and ~1.13 from our α-enhanced and Salaris-corrected modeling, respectively) agrees with the $f_{\nu_{\rm max}}$ determined in Lundkvist et al. (submitted).

5.2.3. *KIC 4671239*

The fundamental parameters of KIC 4671239 were determined in J. R. Larsen et al. (2025) using a BASTA-based modeling procedure. They find a mass of $0.78^{+0.04}_{-0.03}$, a radius of $5.26^{+0.09}_{-0.07}$, and an age of $12.1^{+1.6}_{-1.5}$ Gyr for KIC 4671239. There is close ($< 1\sigma$) agreement between the BASTA modeling results from J. R. Larsen et al. (2025) and the results we determine in this work using both the α-enhanced and Salaris-corrected MESA/GYRE-based modeling (listed in Table 2 and Table 3), though we note that the errors in stellar mass, radius, and particularly age we determine are larger than those determined in J. R. Larsen et al. (2025). J. R. Larsen et al. (2025) determine $f_{\nu_{\rm max}} = 1.101$, which agrees to about 1σ with our determination of $f_{\nu_{\rm max}}$ from our α-enhanced ($f_{\nu_{\rm max}} = 1.07^{+0.03}_{-0.02}$) and Salaris-corrected ($f_{\nu_{\rm max}} = 1.08^{+0.03}_{-0.02}$) modeling.

5.2.4. *KIC 7341231*

S. Deheuvels et al. (2012) calculated best-fit models for KIC 7341231 at varying metallicities ranging from [Z/X] = -1.75 to [Z/X] = -0.75 using the stellar evolution code cesam2k P. Morel (1997). Based on the assumed metallicity, they determine the mass of KIC 7341231 to be in a range between 0.77 and 0.88 $M_\odot$, the radius to be between 2.55 and 2.67 $R_\odot$, and the age range to be between 11.3 and 14.3 Gyr. The mass, radius, and age results of both our α-enhanced and Salaris-corrected listed in Table 2 and Table 3 are within the mass, radius, and age ranges determined in S. Deheuvels et al. (2012).

5.2.5. *KIC 8144907*

D. Huber et al. (2024) carried out asteroseismic modeling of KIC 8144907 using a variety of stellar evolution codes and modeling methods, including MESA/GYRE. Overall, they find a mass of 0.79 ± 0.02 (ran) ± 0.01 (sys), a radius of 3.62 ± 0.04 (ran) ± 0.02 (sys), and an age of 12.0 ± 0.6 (ran) $\pm$ 0.4 (sys) Gyr for KIC 8144907 and also calculate an $f_{\nu_{\rm max}}$ value of 1.056 ± 0.03 based on their best-fit model. Both the stellar mass and radius we find using α-enhanced modeling ($M = 0.737^{+0.023}_{-0.017} M_{\odot}$, $R = 3.516^{+0.032}_{-0.036} R_{\odot}$) are slightly lower than the adopted mass and radius found for KIC 8144907 based on the BeSPP-derived best-fit GARSTEC (A. Weiss & H. Schlattl 2008) model detailed in D. Huber et al. (2024). Consequently, the age we derive from the α-enhanced modeling of KIC 8144907 ($\tau = 14.6^{+1.5}_{-1.3}$ Gyr) is slightly older than the adopted age value from D. Huber et al. (2024). Overall, though, the masses, radii, and ages agree between the works at the 2σ level.

There is also agreement between our Salaris-corrected results for KIC 8144907 and the adopted KIC 8144907 parameters from D. Huber et al. (2024). The Salaris-correction-based modeling procedure produces a mass ($0.752^{+0.026}_{-0.031} M_{\odot}$), radius ($3.538^{+0.048}_{-0.044} R_{\odot}$), and age ($13.9^{+1.9}_{-1.4}$ Gyr) that agree with the results from D. Huber et al. (2024) to within 1σ.

5.2.6. *ν Indi*

W. J. Chaplin et al. (2020) performed detailed asteroseismic modeling of the Halo star ν Indi using just 1 sector of 2-minute cadence data from TESS, yielding 18 mode frequencies. Like D. Huber et al. (2024), multiple methods involving different modeling and oscillation codes were used to find the fundamental parameters of the target star. W. J. Chaplin et al. (2020) reports a mass of $M = 0.85 \pm 0.04$ (stat) $\pm$ 0.02 (sys)$M_{\odot}$ and an age of $\tau = 11 \pm 0.7$ (stat) ± 0.8 (sys) for ν Indi. No radius measurement for ν Indi was reported.

Since ν Indi was observed for more TESS sectors in a faster (20-second) cadence, we used the 20-second data to determine 49 oscillation mode frequencies, more than twice the number of modes compared with W. J. Chaplin et al. (2020) (see Appendix A). Overall, after including the additional asteroseismic data, the masses and ages we determine for ν Indi using our α-enhanced and Salaris-corrected modeling methods still agree to within 1σ errors compared with the mass and age determined for ν Indi in W. J. Chaplin et al. (2020). We find mass results that are slightly smaller than the adopted masses from W. J. Chaplin et al. (2020) (~0.80 $M_{\odot}$ versus 0.85 $M_{\odot}$), and consequently we find a slightly higher age compared with the age adopted in W. J. Chaplin et al. (2020) (~12 Gyr versus 11 Gyr).

6. SUMMARY AND CONCLUSION

In this work, we have conducted a homogeneous asteroseismic modeling of 8 metal-poor stars ([Fe/H] $\lesssim 1.5$) that are enhanced in α-elements ($0.15 \lesssim$ [α/Fe] $\lesssim 0.4$). Our objective was to test two different methods of accounting for α-enhancement and determine if incorporating an α-element-enhanced element mixture with correspondingly α-enhanced opacity tables would result in different derived stellar parameters compared to modeling stars using the widely used global 'Salaris-correction' (M. Salaris et al. 1993) to the observed metallicity.

We performed our asteroseismic modeling of the 8 stars (HD 128279, HD 140283, HD 175305, KIC 4671239, KIC 7341231, KIC 8144907, ν Indi, and TIC 300085386) using the two aforementioned ways of accounting for the α-enhancement when creating stellar models using MESA. In our detailed asteroseismic modeling, we use spectroscopic ([Fe/H], $T_{\rm eff}$, and luminosity measurements) as well as individual mode frequencies from various sources in the literature for all targets in our sample except ν Indi and TIC 300085386 (for which mode frequencies were fitted anew for this work).

From our modeling we find:

1. Comparing the modeling results from our α-enhanced and Salaris-corrected modeling procedures shows that the two different methods of accounting for α-element enhancement in stellar models result in very similar derived stellar masses, radii, and ages.

2. The inferred stellar parameter errors we derive from modeling stars using the Salaris corrections are marginally but consistently larger than errors derived from modeling stars using the full treatment of α-enhancement. Therefore, although the α-enhanced and Salaris-corrected results agree, calculating α-enhanced models with corresponding α-enhanced opacity tables is preferable from a precision standpoint, if such modeling is possible.

3. Our modeling results corroborate recent studies that found that the stellar masses obtained by using only the global asteroseismic parameters are overestimated when compared to masses obtained using detailed asteroseismic modeling (D. Huber et al. 2024; J. R. Larsen et al. 2025; C. J. Lindsay et al. 2025). Using the best-fit results from our homogeneous modeling, we confirm that for metal-poor stars, the $\nu_{\rm max}$ values measured directly from the oscillation power spectra are consistently higher than the $\nu_{\rm max}$ values implied by applying the $\nu_{\rm max}$ scaling relation to the masses, radii, and temperatures obtained from detailed asteroseismic modeling.

4. The close agreement between our modeling results and the stellar parameters derived for the same stars in our sample using different modeling methods shows broadly that asteroseismic modeling produces consistent results at low metallicities even when different modeling codes and methods are used.

These findings are in qualitative disagreement with recent findings that red-giant stellar ages derived from 1D stellar evolution depend strongly on choices of model opacities and abundances (L. M. Morales et al. 2025). Our modeling procedure differs from these works chiefly in the use of individual pulsation-mode frequencies, rather than quantities returned from scaling relations, to constrain the internal structure (rather than global properties) of these red giants. This contributes to the mounting body of evidence that the use of scaling relations alone may not suffice for asteroseismic constraints on stellar properties, in particular ages.

Future asteroseismic studies will produce high-quality light curves for an ever-increasing population of stars across the different Milky Way substructures. With the advent of the Roman Space Telescope (D. Huber et al. 2023; T. J. Weiss et al. 2025) and the PLAnetary Transits and Oscillations of stars mission (PLATO H. Rauer et al. 2022), the asteroseismic study of metal-poor, α-enhanced stars across the Galaxy will benefit from an influx of new data. The asteroseismology of metal-poor, α-enhanced stars will be crucial for unraveling the formation history of the Galaxy's oldest components, such as the stellar halo and thick disk.

We would like to thank M. Lundkvist and J. Larsen for providing the asteroseismic and spectroscopic properties of HD 140283. We would also like to thank A. Stokholm and D. Huber for their helpful discussion. CJL acknowledges support from a Gruber Science Fellowship. CJL and SB acknowledge support from NSF grant AST-2205026. JMJO acknowledges support from NASA through the NASA Hubble Fellowship grant HST-HF2-51517.001, awarded by the Space Telescope Science Institute (STScI). S.G. acknowledges support by the National Aeronautics and Space Administration under grants 80NSSC23K0137 and 80NSSC23K0168 issued through the TESS Guest Investigator Program. M.H. acknowledges support from NASA grant 80NSSC24K0228. We acknowledge the use of public TESS data from pipelines at the TESS Science Office and at the TESS Science Processing Operations Center. This research has made use of the Exoplanet Follow-up Observation Program website, which is operated by the California Institute of Technology under contract with the National Aeronautics and Space Administration under the Exoplanet Exploration Program. Funding for the TESS mission is provided by NASA's Science Mission Directorate.

Software: MESA (B. Paxton et al. 2011, 2013, 2015, 2018, 2019; A. S. Jermyn et al. 2023), GYRE (R. H. D. Townsend & S. A. Teitler 2013) , SciPy (P. Virtanen et al. 2020), Pandas (J. Reback et al. 2021), Astropy (Astropy Collaboration et al. 2013, 2018, 2022), Lightkurve (Lightkurve Collaboration et al. 2018), `PBJam` (M. B. Nielsen et al. 2021, 2025), `reggae` (J. Ong et al. 2024), TACO (N. Themeßl et al. 2020), YABOX (P. R. Mier 2017), corner.py (D. Foreman-Mackey 2017)

Example MESA and GYRE inlists we used to generate our models and calculate model frequencies are archived on Zenodo and can be downloaded at https://zenodo.org/records/16995052. We also include the MESA evolutionary tracks and profiles for our best-fit models.

REFERENCES

Abdurro'uf, Accetta, K., Aerts, C., et al. 2022, The Seventeenth Data Release of the Sloan Digital Sky Surveys: Complete Release of MaNGA, MaStar, and APOGEE-2 Data, ApJS, 259, 35, doi: 10.3847/1538-4365/ac4414

Alencastro Puls, A., Casagrande, L., Monty, S., et al. 2022, Chemo-dynamics and asteroseismic ages of seven metal-poor red giants from the Kepler field, MNRAS, 510, 1733, doi: 10.1093/mnras/stab3545

Alongi, M., Bertelli, G., Bressan, A., & Chiosi, C. 1991, Effects of envelope overshoot on stellar models., A&A, 244, 95

Astropy Collaboration, Robitaille, T. P., Tollerud, E. J., et al. 2013, Astropy: A community Python package for astronomy, A&A, 558, A33, doi: 10.1051/0004-6361/201322068

Astropy Collaboration, Price-Whelan, A. M., Sipőcz, B. M., et al. 2018, The Astropy Project: Building an Open-science Project and Status of the v2.0 Core Package, AJ, 156, 123, doi: 10.3847/1538-3881/aabc4f

Astropy Collaboration, Price-Whelan, A. M., Lim, P. L., et al. 2022, The Astropy Project: Sustaining and Growing a Community-oriented Open-source Project and the Latest Major Release (v5.0) of the Core Package, ApJ, 935, 167, doi: 10.3847/1538-4357/ac7c74

Baglin, A., Auvergne, M., Barge, P., et al. 2006, in ESA Special Publication, Vol. 1306, The CoRoT Mission Pre-Launch Status - Stellar Seismology and Planet Finding, ed. M. Fridlund, A. Baglin, J. Lochard, & L. Conroy, 33

Ball, W. H., & Gizon, L. 2014, A new correction of stellar oscillation frequencies for near-surface effects, A&A, 568, A123, doi: 10.1051/0004-6361/201424325

Basu, S., & Chaplin, W. J. 2017, Asteroseismic Data Analysis: Foundations and Techniques

Basu, S., & Kinnane, A. 2018, The Robustness of Asteroseismic Estimates of Global Stellar Parameters to Surface Term Corrections, ApJ, 869, 8, doi: 10.3847/1538-4357/aae922

Bellinger, E. P., Hekker, S., Angelou, G. C., Stokholm, A., & Basu, S. 2019, Stellar ages, masses, and radii from asteroseismic modeling are robust to systematic errors in spectroscopy, A&A, 622, A130, doi: 10.1051/0004-6361/201834461

Borre, C. C., Aguirre Børsen-Koch, V., Helmi, A., et al. 2022, Age determination of galaxy merger remnant stars using asteroseismology, MNRAS, 514, 2527, doi: 10.1093/mnras/stac1498

Borucki, W. J., Koch, D., Basri, G., et al. 2010, Kepler Planet-Detection Mission: Introduction and First Results, Science, 327, 977, doi: 10.1126/science.1185402

Brown, T. M., Gilliland, R. L., Noyes, R. W., & Ramsey, L. W. 1991, Detection of Possible p-Mode Oscillations on Procyon, ApJ, 368, 599, doi: 10.1086/169725

Chaplin, W. J., Serenelli, A. M., Miglio, A., et al. 2020, Age dating of an early Milky Way merger via asteroseismology of the naked-eye star ν Indi, Nature Astronomy, 4, 382, doi: 10.1038/s41550-019-0975-9

Cunha, M. S., Roxburgh, I. W., Aguirre Børsen-Koch, V., et al. 2021, PLATO hare-and-hounds exercise: asteroseismic model fitting of main-sequence solar-like pulsators, MNRAS, 508, 5864, doi: 10.1093/mnras/stab2886

de Brito Silva, D., Jofré, P., Worley, C., Hawkins, K., & Das, P. 2024, The accreted galaxy: An overview of TESS metal-poor accreted star candidates, A&A, 690, A120, doi: 10.1051/0004-6361/202450610

Deheuvels, S., & Michel, E. 2011, Constraints on the structure of the core of subgiants via mixed modes: the case of HD 49385, A&A, 535, A91, doi: 10.1051/0004-6361/201117232

Deheuvels, S., García, R. A., Chaplin, W. J., et al. 2012, Seismic Evidence for a Rapidly Rotating Core in a Lower-giant-branch Star Observed with Kepler, ApJ, 756, 19, doi: 10.1088/0004-637X/756/1/19

Epstein, C. R., Elsworth, Y. P., Johnson, J. A., et al. 2014, Testing the Asteroseismic Mass Scale Using Metal-poor Stars Characterized with APOGEE and Kepler, ApJL, 785, L28, doi: 10.1088/2041-8205/785/2/L28

Foreman-Mackey, D. 2017, corner.py: Corner plots,, Astrophysics Source Code Library, record ascl:1702.002

Gaia Collaboration, Prusti, T., de Bruijne, J. H. J., et al. 2016, The Gaia mission, A&A, 595, A1, doi: 10.1051/0004-6361/201629272

Gaia Collaboration, Brown, A. G. A., Vallenari, A., et al. 2018, Gaia Data Release 2. Summary of the contents and survey properties, A&A, 616, A1, doi: 10.1051/0004-6361/201833051

Gaia Collaboration, Brown, A. G. A., Vallenari, A., et al. 2021, Gaia Early Data Release 3. Summary of the contents and survey properties, A&A, 649, A1, doi: 10.1051/0004-6361/202039657

Gallart, C., Surot, F., Cassisi, S., et al. 2024, Chronology of our Galaxy from Gaia colour-magnitude diagram fitting (ChronoGal). I. The formation and evolution of the thin disc from the Gaia Catalogue of Nearby Stars, A&A, 687, A168, doi: 10.1051/0004-6361/202349078

Ge, Z. S., Bi, S. L., Li, T. D., et al. 2015, Asteroseismic analysis of two α-enhanced stars KIC 7976303 and KIC 8694723, MNRAS, 447, 680, doi: 10.1093/mnras/stu2391

Grevesse, N., & Sauval, A. J. 1998, Standard Solar Composition, SSRv, 85, 161, doi: 10.1023/A:1005161325181

Grunblatt, S. K., Zinn, J. C., Price-Whelan, A. M., et al. 2021, Age-dating Red Giant Stars Associated with Galactic Disk and Halo Substructures, ApJ, 916, 88, doi: 10.3847/1538-4357/ac0532

Grunblatt, S. K., Saunders, N., Sun, M., et al. 2022, TESS Giants Transiting Giants. II. The Hottest Jupiters Orbiting Evolved Stars, AJ, 163, 120, doi: 10.3847/1538-3881/ac4972

Grunblatt, S. K., Saunders, N., Chontos, A., et al. 2023, TESS Giants Transiting Giants. III. An Eccentric Warm Jupiter Supports a Period-Eccentricity Relation for Giant Planets Transiting Evolved Stars, AJ, 165, 44, doi: 10.3847/1538-3881/aca670

Grunblatt, S. K., Saunders, N., Huber, D., et al. 2024, TESS Giants Transiting Giants. IV. A Low-density Hot Neptune Orbiting a Red Giant Star, AJ, 168, 1, doi: 10.3847/1538-3881/ad4149

Hekker, S., & Christensen-Dalsgaard, J. 2017, Giant star seismology, A&A Rv, 25, 1, doi: 10.1007/s00159-017-0101-x

Helmi, A., Babusiaux, C., Koppelman, H. H., et al. 2018, The merger that led to the formation of the Milky Way's inner stellar halo and thick disk, Nature, 563, 85, doi: 10.1038/s41586-018-0625-x

Helmi, A., White, S. D. M., de Zeeuw, P. T., & Zhao, H. 1999, Debris streams in the solar neighbourhood as relicts from the formation of the Milky Way, Nature, 402, 53, doi: 10.1038/46980

Huber, D., White, T. R., Metcalfe, T. S., et al. 2022, A 20 Second Cadence View of Solar-type Stars and Their Planets with TESS: Asteroseismology of Solar Analogs and a Recharacterization of π Men c, AJ, 163, 79, doi: 10.3847/1538-3881/ac3000

Huber, D., Pinsonneault, M., Beck, P., et al. 2023, Asteroseismology with the Roman Galactic Bulge Time-Domain Survey, arXiv e-prints, arXiv:2307.03237, doi: 10.48550/arXiv.2307.03237

Huber, D., Slumstrup, D., Hon, M., et al. 2024, Stellar Models are Reliable at Low Metallicity: An Asteroseismic Age for the Ancient Very Metal-poor Star KIC 8144907, ApJ, 975, 19, doi: 10.3847/1538-4357/ad7110

Ishigaki, M. N., Chiba, M., & Aoki, W. 2012, Chemical Abundances of the Milky Way Thick Disk and Stellar Halo. I. Implications of [α/Fe] for Star Formation Histories in Their Progenitors, ApJ, 753, 64, doi: 10.1088/0004-637X/753/1/64

Jermyn, A. S., Bauer, E. B., Schwab, J., et al. 2023, Modules for Experiments in Stellar Astrophysics (MESA): Time-dependent Convection, Energy Conservation, Automatic Differentiation, and Infrastructure, ApJS, 265, 15, doi: 10.3847/1538-4365/acae8d

Karovicova, I., White, T. R., Nordlander, T., et al. 2020, Fundamental stellar parameters of benchmark stars from CHARA interferometry. I. Metal-poor stars, A&A, 640, A25, doi: 10.1051/0004-6361/202037590

Khan, S., Hall, O. J., Miglio, A., et al. 2018, The Red-giant Branch Bump Revisited: Constraints on Envelope Overshooting in a Wide Range of Masses and Metallicities, ApJ, 859, 156, doi: 10.3847/1538-4357/aabf90

Kjeldsen, H., & Bedding, T. R. 1995, Amplitudes of stellar oscillations: the implications for asteroseismology., A&A, 293, 87. https://arxiv.org/abs/astro-ph/9403015

Kobayashi, C., Karakas, A. I., & Lugaro, M. 2020, The Origin of Elements from Carbon to Uranium, ApJ, 900, 179, doi: 10.3847/1538-4357/abae65

Koppelman, H. H., Helmi, A., Massari, D., Roelenga, S., & Bastian, U. 2019, Characterization and history of the Helmi streams with Gaia DR2, A&A, 625, A5, doi: 10.1051/0004-6361/201834769

Kuszlewicz, J. S., Hon, M., & Huber, D. 2023, Mixed-mode Ensemble Asteroseismology of Low-luminosity Kepler Red Giants, ApJ, 954, 152, doi: 10.3847/1538-4357/ace598

Larsen, J. R., Rørsted, J. L., Aguirre Børsen-Koch, V., et al. 2025, Pushing the boundaries of asteroseismic individual frequency modelling: Unveiling two evolved very low-metallicity red giants, A&A, 697, A153, doi: 10.1051/0004-6361/202453554

Li, T., Li, Y., Bi, S., et al. 2022, Asteroseismology of 3642 Kepler Red Giants: Correcting the Scaling Relations Based on Detailed Modeling, ApJ, 927, 167, doi: 10.3847/1538-4357/ac4fbf

Li, Y., & Joyce, M. 2025, Beyond MESA Defaults: The Impact of Structural Resolution Uncertainty in p-mode Asteroseismology, arXiv e-prints, arXiv:2501.13207, doi: 10.48550/arXiv.2501.13207

Li, Y., Bedding, T. R., Stello, D., et al. 2023, A prescription for the asteroseismic surface correction, MNRAS, 523, 916, doi: 10.1093/mnras/stad1445

Li, Y., Bedding, T. R., Huber, D., et al. 2024, Realistic Uncertainties for Fundamental Properties of Asteroseismic Red Giants and the Interplay between Mixing Length, Metallicity, and ¡inline-formula¿ ¡mml:math overflow="scroll"¿¡mml:msub¿¡mml:mrow¿¡mml:mi¿ν¡/mml:mi¿¡/mml:mrow ¡/inline-formula¿, ApJ, 974, 77, doi: 10.3847/1538-4357/ad6c3e

Lightkurve Collaboration, Cardoso, J. V. d. M. a., Hedges, C., et al. 2018, Lightkurve: Kepler and TESS time series analysis in Python, http://ascl.net/1812.013

Lindsay, C. J., Ong, J. M. J., & Basu, S. 2022, Mixed-mode Asteroseismology of Red Giant Stars Through the Luminosity Bump, ApJ, 931, 116, doi: 10.3847/1538-4357/ac67ed

Lindsay, C. J., Ong, J. M. J., & Basu, S. 2024, Fossil Signatures of Main-sequence Convective Core Overshoot Estimated through Asteroseismic Analyses, ApJ, 965, 171, doi: 10.3847/1538-4357/ad2ae5

Lindsay, C. J., Hon, M., Ong, J. M. J., et al. 2025, Precise Asteroseismic Ages for the Helmi Streams, ApJ, 989, 189, doi: 10.3847/1538-4357/adeb56

Majewski, S. R., APOGEE Team, & APOGEE-2 Team. 2016, The Apache Point Observatory Galactic Evolution Experiment (APOGEE) and its successor, APOGEE-2, Astronomische Nachrichten, 337, 863, doi: 10.1002/asna.201612387

Marasco, C., Tayar, J., & Nidever, D. 2025, Asteroseismology of Metal-Poor Red Giants Observed by TESS, arXiv e-prints, arXiv:2504.18642, doi: 10.48550/arXiv.2504.18642

McWilliam, A., Preston, G. W., Sneden, C., & Searle, L. 1995, Spectroscopic Analysis of 33 of the Most Metal Poor Stars. II., AJ, 109, 2757, doi: 10.1086/117486

Mier, P. R. 2017, pablormier/yabox: v1.0.3,, v1.0.3 Zenodo, doi: 10.5281/zenodo.848679

Miglio, A., Chiappini, C., Mackereth, J. T., et al. 2021, Age dissection of the Milky Way discs: Red giants in the Kepler field, A&A, 645, A85, doi: 10.1051/0004-6361/202038307

Morales, L. M., Tayar, J., & Claytor, Z. R. 2025, Model Choice Matters for Age Inference on the Red Giant Branch, ApJ, 986, 229, doi: 10.3847/1538-4357/add2f5

Morel, P. 1997, CESAM: A code for stellar evolution calculations, A&AS, 124, 597, doi: 10.1051/aas:1997209

Nielsen, M. B., Davies, G. R., Ball, W. H., et al. 2021, PBjam: A Python Package for Automating Asteroseismology of Solar-like Oscillators, AJ, 161, 62, doi: 10.3847/1538-3881/abcd39

Nielsen, M. B., Ong, J. M. J., Hatt, E. J., et al. 2025, Asteroseismology with PBjam 2.0: Measuring Dipole Mode Frequencies in Coupling Regimes from Main-sequence to Low-luminosity Red Giant Stars, AJ, 169, 322, doi: 10.3847/1538-3881/adcb37

Nissen, P. E., & Schuster, W. J. 2010, Two distinct halo populations in the solar neighborhood. Evidence from stellar abundance ratios and kinematics, A&A, 511, L10, doi: 10.1051/0004-6361/200913877

Ong, J., Nielsen, M., Hatt, E., & Davies, G. 2024, Reggae: A Parametric Tuner for PBJam, and a Visualization Tool for Red Giant Oscillation Spectra, The Journal of Open Source Software, 9, 6588, doi: 10.21105/joss.06588

Ong, J. M. J., & Basu, S. 2020, Semianalytic Expressions for the Isolation and Coupling of Mixed Modes, ApJ, 898, 127, doi: 10.3847/1538-4357/ab9ffb

Ong, J. M. J., Basu, S., & McKeever, J. M. 2021, Differential Modeling Systematics across the HR Diagram from Asteroseismic Surface Corrections, ApJ, 906, 54, doi: 10.3847/1538-4357/abc7c1

Paxton, B., Bildsten, L., Dotter, A., et al. 2011, Modules for Experiments in Stellar Astrophysics (MESA), ApJS, 192, 3, doi: 10.1088/0067-0049/192/1/3

Paxton, B., Cantiello, M., Arras, P., et al. 2013, Modules for Experiments in Stellar Astrophysics (MESA): Planets, Oscillations, Rotation, and Massive Stars, ApJS, 208, 4, doi: 10.1088/0067-0049/208/1/4

Paxton, B., Marchant, P., Schwab, J., et al. 2015, Modules for Experiments in Stellar Astrophysics (MESA): Binaries, Pulsations, and Explosions, ApJS, 220, 15, doi: 10.1088/0067-0049/220/1/15

Paxton, B., Schwab, J., Bauer, E. B., et al. 2018, Modules for Experiments in Stellar Astrophysics (MESA): Convective Boundaries, Element Diffusion, and Massive Star Explosions, ApJS, 234, 34, doi: 10.3847/1538-4365/aaa5a8

Paxton, B., Smolec, R., Schwab, J., et al. 2019, Modules for Experiments in Stellar Astrophysics (MESA): Pulsating Variable Stars, Rotation, Convective Boundaries, and Energy Conservation, ApJS, 243, 10, doi: 10.3847/1538-4365/ab2241

Pereira, F., Grunblatt, S. K., Psaridi, A., et al. 2024, TESS giants transiting giants V - two hot Jupiters orbiting red giant hosts, MNRAS, 527, 6332, doi: 10.1093/mnras/stad3449

Pinsonneault, M. H., Elsworth, Y. P., Tayar, J., et al. 2018, The Second APOKASC Catalog: The Empirical Approach, ApJS, 239, 32, doi: 10.3847/1538-4365/aaebfd

Pinsonneault, M. H., Zinn, J. C., Tayar, J., et al. 2025, APOKASC-3: The Third Joint Spectroscopic and Asteroseismic Catalog for Evolved Stars in the Kepler Fields, ApJS, 276, 69, doi: 10.3847/1538-4365/ad9fef

Planck Collaboration, Aghanim, N., Akrami, Y., et al. 2020, Planck 2018 results. VI. Cosmological parameters, A&A, 641, A6, doi: 10.1051/0004-6361/201833910

Rauer, H., Aerts, C., Deleuil, M., et al. 2022, in European Planetary Science Congress, EPSC2022–453, doi: 10.5194/epsc2022-453

Reback, J., Mendel, J. B., McKinney, W., et al. 2021, pandas-dev/pandas: Pandas 1.3.0,, v1.3.0 Zenodo, doi: 10.5281/zenodo.3509134

Ricker, G. R., Winn, J. N., Vanderspek, R., et al. 2015, Transiting Exoplanet Survey Satellite (TESS), Journal of Astronomical Telescopes, Instruments, and Systems, 1, 014003, doi: 10.1117/1.JATIS.1.1.014003

Ruiz-Lara, T., Helmi, A., Gallart, C., Surot, F., & Cassisi, S. 2022, Unveiling the past evolution of the progenitor of the Helmi streams, A&A, 668, L10, doi: 10.1051/0004-6361/202244127

Salaris, M., Chieffi, A., & Straniero, O. 1993, The alpha -enhanced Isochrones and Their Impact on the FITS to the Galactic Globular Cluster System, ApJ, 414, 580, doi: 10.1086/173105

Saunders, N., Grunblatt, S. K., Huber, D., et al. 2022, TESS Giants Transiting Giants. I.: A Noninflated Hot Jupiter Orbiting a Massive Subgiant, AJ, 163, 53, doi: 10.3847/1538-3881/ac38a1

Saunders, N., Grunblatt, S. K., Chontos, A., et al. 2024, TESS Giants Transiting Giants. VI. Newly Discovered Hot Jupiters Provide Evidence for Efficient Obliquity Damping after the Main Sequence, AJ, 168, 81, doi: 10.3847/1538-3881/ad543b

Saunders, N., Grunblatt, S. K., Huber, D., et al. 2025a, Giants: Pipeline to search for exoplanets around evolved stars,, Astrophysics Source Code Library, record ascl:2502.006

Saunders, N., Grunblatt, S. K., Huber, D., et al. 2025b, TESS Giants Transiting Giants. VII. A Hot Saturn Orbiting an Oscillating Red Giant Star, AJ, 169, 75, doi: 10.3847/1538-3881/ad9a87

Sharma, S., Stello, D., Bland-Hawthorn, J., Huber, D., & Bedding, T. R. 2016, Stellar Population Synthesis Based Modeling of the Milky Way Using Asteroseismology of 13,000 Kepler Red Giants, ApJ, 822, 15, doi: 10.3847/0004-637X/822/1/15

Silva Aguirre, V., Davies, G. R., Basu, S., et al. 2015, Ages and fundamental properties of Kepler exoplanet host stars from asteroseismology, MNRAS, 452, 2127, doi: 10.1093/mnras/stv1388

Silva Aguirre, V., Bojsen-Hansen, M., Slumstrup, D., et al. 2018, Confirming chemical clocks: asteroseismic age dissection of the Milky Way disc(s), MNRAS, 475, 5487, doi: 10.1093/mnras/sty150

Soderblom, D. R. 2010, The Ages of Stars, ARA&A, 48, 581, doi: 10.1146/annurev-astro-081309-130806

Soderblom, D. R. 2014, in Search for Life Beyond the Solar System. Exoplanets, Biosignatures & Instruments, ed. D. Apai & P. Gabor, 2.17

Spite, M., & Spite, F. 1978, Nucleosynthesis in the Galaxy and the chemical composition of old halo stars., A&A, 67, 23

Stokholm, A., Aguirre Børsen-Koch, V., Stello, D., Hon, M., & Reyes, C. 2023, A unified exploration of the chronology of the Galaxy, MNRAS, 524, 1634, doi: 10.1093/mnras/stad1912

Sun, T., Ge, Z., Chen, X., et al. 2023, Age of FGK Dwarfs Observed with LAMOST and GALAH: Considering the Oxygen Enhancement, ApJS, 268, 29, doi: 10.3847/1538-4365/ace5b0

Tassoul, M. 1980, Asymptotic approximations for stellar nonradial pulsations., ApJS, 43, 469, doi: 10.1086/190678

Themeßl, N., Kuszlewicz, J. S., García Saravia Ortiz de Montellano, A., & Hekker, S. 2020, in Stars and their Variability Observed from Space, ed. C. Neiner, W. W. Weiss, D. Baade, R. E. Griffin, C. C. Lovekin, & A. F. J. Moffat, 287–291

Thoul, A. A., Bahcall, J. N., & Loeb, A. 1994, Element Diffusion in the Solar Interior, ApJ, 421, 828, doi: 10.1086/173695

Tinsley, B. M. 1980, Evolution of the Stars and Gas in Galaxies, FCPh, 5, 287, doi: 10.48550/arXiv.2203.02041

Townsend, R. H. D., & Teitler, S. A. 2013, GYRE: an open-source stellar oscillation code based on a new Magnus Multiple Shooting scheme, MNRAS, 435, 3406, doi: 10.1093/mnras/stt1533

Valle, G., Dell'Omodarme, M., Prada Moroni, P. G., & Degl'Innocenti, S. 2024, Impact of α enhancement on the asteroseismic age determination of field stars. Application to the APO-K2 catalogue, arXiv e-prints, arXiv:2403.03070, doi: 10.48550/arXiv.2403.03070

Virtanen, P., Gommers, R., Oliphant, T. E., et al. 2020, SciPy 1.0: fundamental algorithms for scientific computing in Python, Nature Methods, 17, 261, doi: 10.1038/s41592-019-0686-2

Warfield, J. T., Zinn, J. C., Pinsonneault, M. H., et al. 2021, An Intermediate-age Alpha-rich Galactic Population in K2, AJ, 161, 100, doi: 10.3847/1538-3881/abd39d

Warfield, J. T., Zinn, J. C., Schonhut-Stasik, J., et al. 2024, The APO-K2 Catalog. II. Accurate Stellar Ages for Red Giant Branch Stars across the Milky Way, AJ, 167, 208, doi: 10.3847/1538-3881/ad33bb

Weiss, A., & Schlattl, H. 2008, GARSTEC—the Garching Stellar Evolution Code. The direct descendant of the legendary Kippenhahn code, Ap&SS, 316, 99, doi: 10.1007/s10509-007-9606-5

Weiss, T. J., Downing, N. J., Pinsonneault, M. H., et al. 2025, Modeling Asteroseismic Yields for the Roman Galactic Bulge Time-domain Survey, ApJ, 987, 181, doi: 10.3847/1538-4357/adde5b

Wilson, J. C., Hearty, F. R., Skrutskie, M. F., et al. 2019, The Apache Point Observatory Galactic Evolution Experiment (APOGEE) Spectrographs, PASP, 131, 055001, doi: 10.1088/1538-3873/ab0075

Xiang, M., & Rix, H.-W. 2022, A time-resolved picture of our Milky Way's early formation history, Nature, 603, 599, doi: 10.1038/s41586-022-04496-5

Yu, J., Huber, D., Bedding, T. R., et al. 2018, Asteroseismology of 16,000 Kepler Red Giants: Global Oscillation Parameters, Masses, and Radii, ApJS, 236, 42, doi: 10.3847/1538-4365/aaaf74

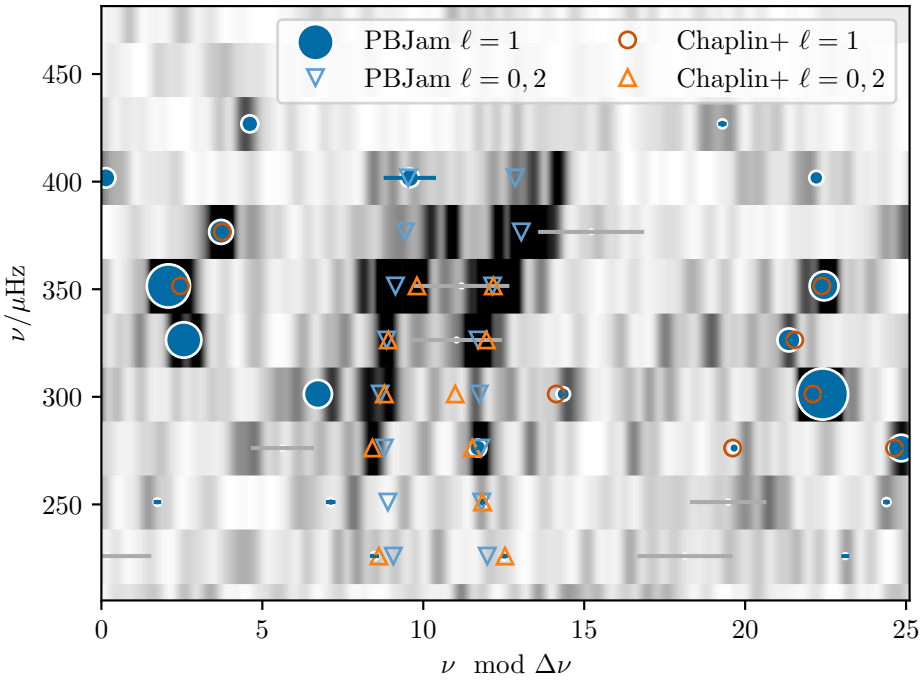

Figure 9. Échelle diagram (frequency versus frequency mod large frequency separation) showing modes fitted against the 20-second cadence ν Indi TESS data. The radial and quadrupole p-mode frequencies we fitted using `PBJam` are shown with blue triangles and the dipolar mixed-mode frequencies we fitted using `reggae` are shown with blue circles. The size of the blue circle represents the fitted mixed-mode amplitude. Grey intervals show where `reggae` predicts dipole modes which either are too low in amplitude, or lie too close to an even-degree mode, to permit unambiguous identification and constraints from the power spectrum. The background heat-map shows the power spectrum of ν Indi, and the orange markers show the $\ell = 0, 1$ and 2 modes identified in W. J. Chaplin et al. (2020) using sine-wave fitting in the time domain.

APPENDIX

A. INDIVIDUAL MODE FREQUENCY DETERMINATION FOR ν INDI

Previous asteroseismic studies of ν-Indi used only 27 days (one sector) of TESS data (W. J. Chaplin et al. 2020), taken at an observational cadence of 120 s. Since then, 5 additional 27-day-long sectors of TESS observations have been taken of ν-Indi. For two of these sectors, sector 67 and sector 68, ν-Indi was observed in 20-second cadence. 20-second cadence data allows for improved precision compared to 120 second data (D. Huber et al. 2022).

In order to determine the individual mode frequencies from the TESS timeseries, we first stitched the 20-second cadence data from sectors 67 and 68 together using the `Lightkurve` package (Lightkurve Collaboration et al. 2018). Then, after calculating the power spectra of the stitched lightcurve, the radial and quadrupole ($\ell = 0, 2$) p-mode frequencies were calculated using the open-source peak-bagging package `PBJam` (M. B. Nielsen et al. 2021). Mode identifications for the radial and quadrupole frequencies were validated using a different peak-bagging code, `TACO` (N. Themeßl et al. 2020). The dipolar ($\ell = 1$) mixed mode frequencies were identified and fitted using `reggae`, which implements a generative model for the $\ell = 1$ mixed modes using the π- and γ-mode parameterization described in J. M. J. Ong & S. Basu (2020). The p-mode and mixed-mode frequencies are listed in Table 6 and shown in Figure 9 along with the previously identified modes from W. J. Chaplin et al. (2020).

B. INDIVIDUAL MODE FREQUENCY DETERMINATION FOR TIC 300085386

The global asteroseismic parameters and individual oscillation mode frequencies were determined from the TESS observations using the peak-bagging code TACO (N. Themeßl et al. 2020). TIC 300085386 was observed for numerous sectors due to its position in the southern continuous viewing zone. We used the `giants` pipeline (N. Saunders et al. 2025a) to produce noise-corrected TESS light curves following the de-trending procedure described in Section 2.2 of N. Saunders et al. (2022) and smoothing procedure described in Section 3.3 of S. K. Grunblatt et al. (2021). The `giants` pipeline was designed for the

detection of transiting planet (S. K. Grunblatt et al. 2022, 2023, 2024; F. Pereira et al. 2024; N. Saunders et al. 2024, 2025b) and asteroseismic (S. K. Grunblatt et al. 2021, 2022; N. Saunders et al. 2025b) signals in the light curves of evolved stars, Then, the global asteroseismic parameters, $\Delta\nu$ and $\nu_{\rm max}$ were calculated using TACO by first calculating a power density spectrum (PDS) from the light curve, dividing out the background components arising from convective granulation and white noise, then finding the frequency of maximum oscillation power ($\nu_{\rm max}$). Oscillation peaks are then identified from the power density spectrum by applying a Mexican-hat wavelet-transform based algorithm to iteratively find resolved peaks. The peaks are then fitted with Lorentzian functions to determine the frequencies and frequency uncertainties.

The p-mode oscillation modes ($\ell = 0$ and $\ell = 2$) are identified using the universal pattern for p-mode oscillations of the same angular degree, $\nu_{n_p,\ell,m} \sim \Delta\nu(n_p + \frac{\ell}{2} + \epsilon_p)$, where $\Delta\nu$ is the large frequency spacing, ϵ_p is a phase term, and n_p, ℓ, and m are the p-mode radial order, angular degree, and azimuthal order respectively (M. Tassoul 1980). The large frequency spacing is identified by TACO using the spacing in frequency between $\ell = 0$ p-modes of consecutive radial order. For the peaks not identified using the universal pattern as $\ell = 0$ or $\ell = 2$ modes, TACO identifies them as dipole modes ($\ell = 1$). The frequencies, frequency errors, and angular degrees for the oscillation modes of TIC 300085386 are reported in Table 7.

ℓ	ν [μHz]	σ_ν [μHz]
0	237.970	0.745
0	262.907	0.736
0	287.988	0.658
0	313.046	0.646
0	338.120	0.075
0	363.679	0.192
0	389.679	0.386
0	414.600	0.711
1	234.490	0.146
1	238.509	0.099
1	249.096	0.148
1	252.821	0.134
1	258.203	0.167
1	262.951	0.064
1	275.465	0.105
1	287.892	0.073
1	295.871	0.089
1	301.048	0.072
1	308.016	0.313
1	315.652	0.099
1	323.716	0.044
1	328.979	0.059
1	347.780	0.063
1	353.605	0.049
1	373.979	0.060
1	380.353	0.056
1	401.870	0.123
1	411.280	0.803
1	423.953	0.100
1	431.473	0.085
1	446.132	0.145
2	235.050	0.768
2	259.990	0.755
2	284.989	0.696
2	309.971	0.360
2	335.279	0.222
2	360.661	0.565
2	386.077	0.729
2	411.276	0.758

Table 6. ν-Indi mode frequencies extracted from the two sectors of 20-second cadence TESS data.

ℓ	ν [μHz]	σ_ν [μHz]
0	46.832	0.007
0	53.237	0.015
0	59.809	0.078
0	66.485	0.007
0	73.276	0.007
1	50.006	0.120
1	50.127	0.045
1	50.260	0.059
1	56.143	0.210
1	56.352	0.055
1	56.525	0.056
1	56.719	0.108
1	56.890	0.100
1	62.663	0.059
1	62.897	0.070
1	63.128	0.296
1	63.332	0.057
1	63.561	0.070
1	69.812	0.065
1	70.118	0.099
1	76.647	0.199
1	76.868	0.207
2	45.881	0.008
2	52.212	0.016
2	58.889	0.015
2	65.409	0.021

Table 7. TIC 300085386 mode frequencies extracted from 30-minute cadence TESS data.

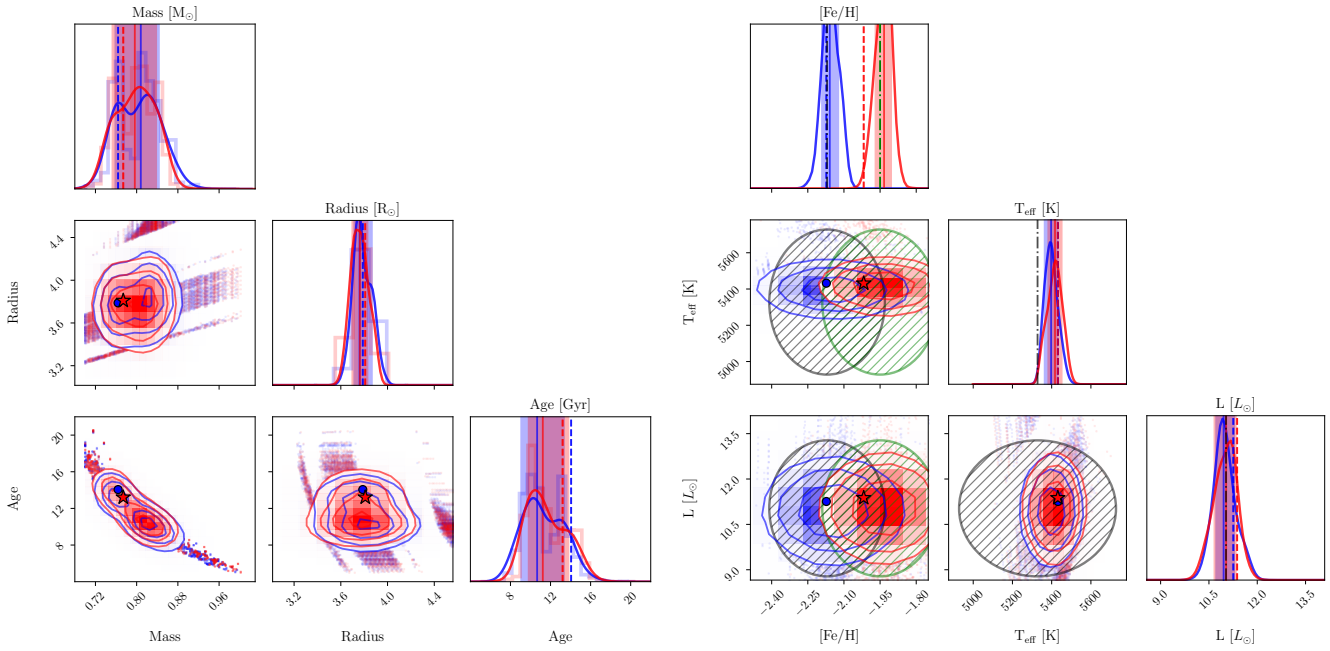

Figure 10. Left panel shows the global parameter corner plot similar to Figure 3 except for HD 128279. The right panel shows the spectroscopic parameter corner plot similar to Figure 4 except for HD 128279.

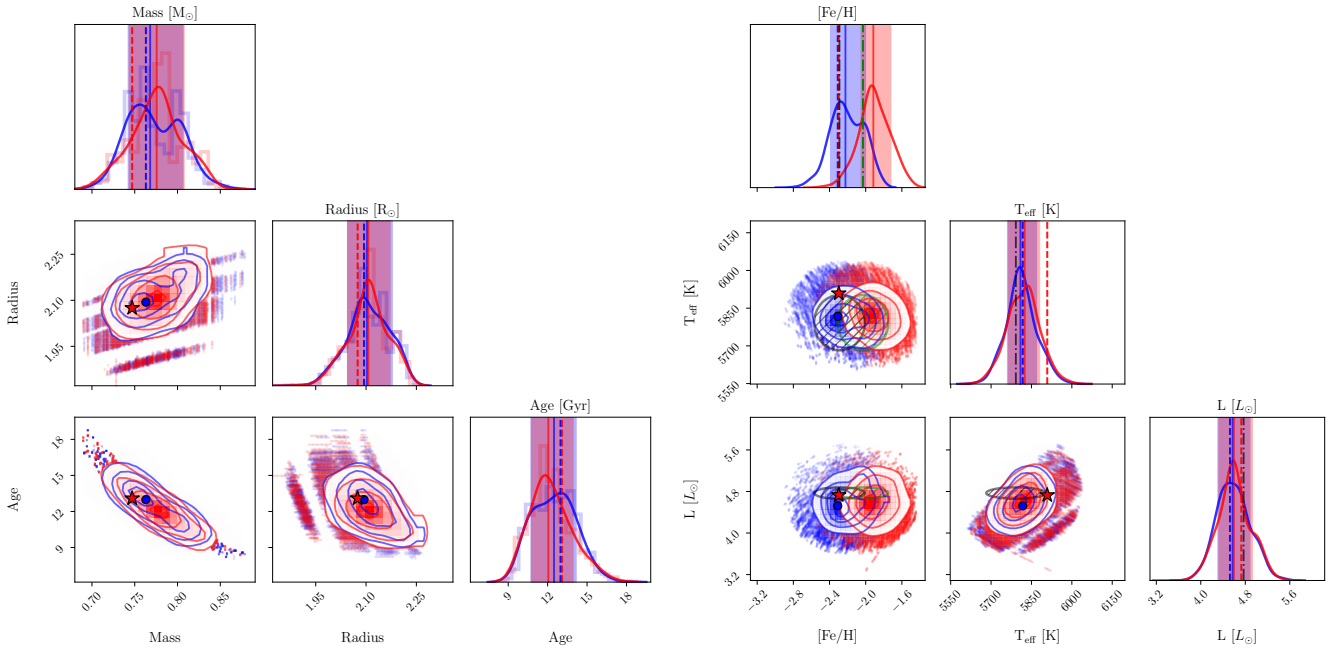

Figure 11. Same as Figure 10 except for HD 140283.

C. CORNER PLOTS

Figure 10, Figure 11, Figure 12, Figure 13, Figure 14, Figure 15, andFigure 16, show the global parameter and spectroscopic parameter corner plots similar to Figure 3 and Figure 4 for the other stars in our sample. See section 3 for a description of each corner plot's construction.

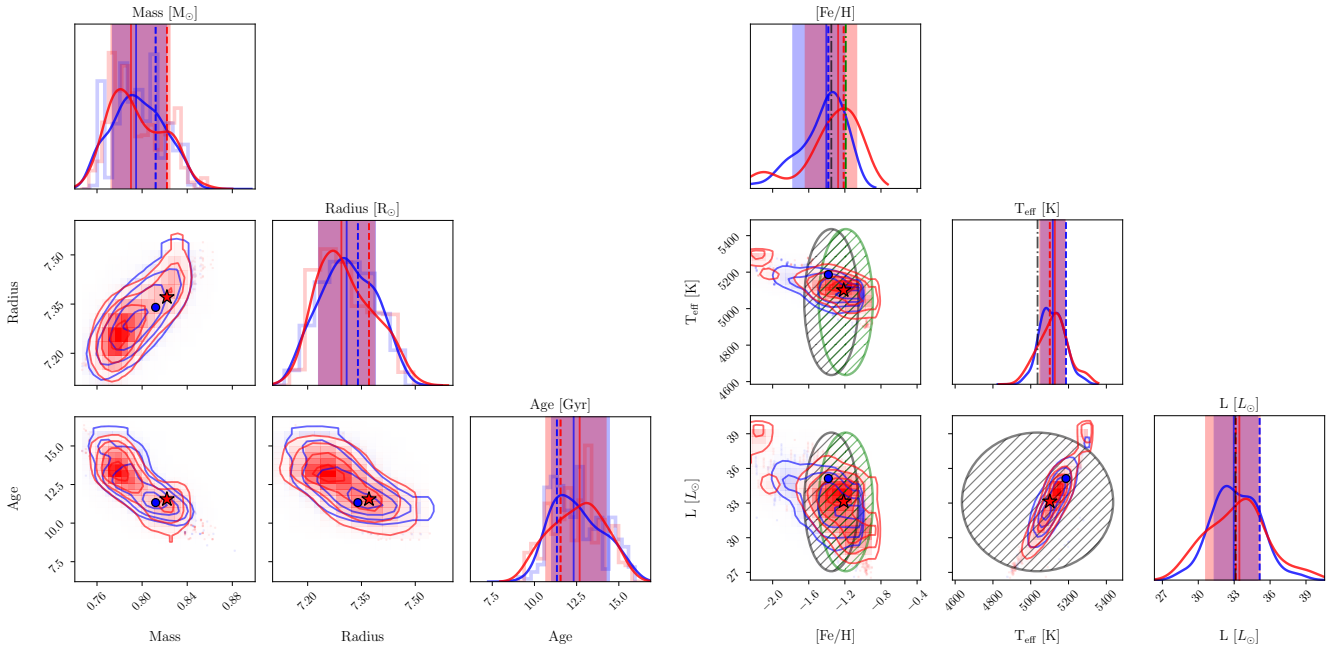

Figure 12. Same as Figure 10 except for HD 175305.

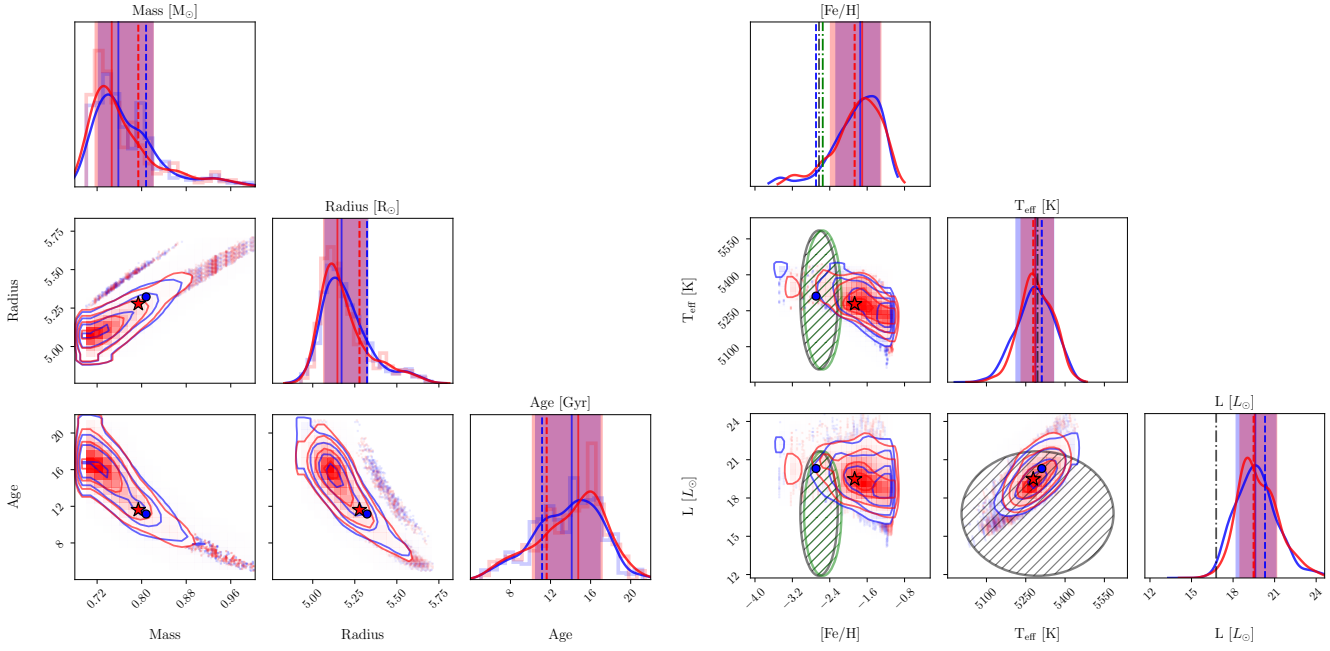

Figure 13. Same as Figure 10 except for KIC 4671239.

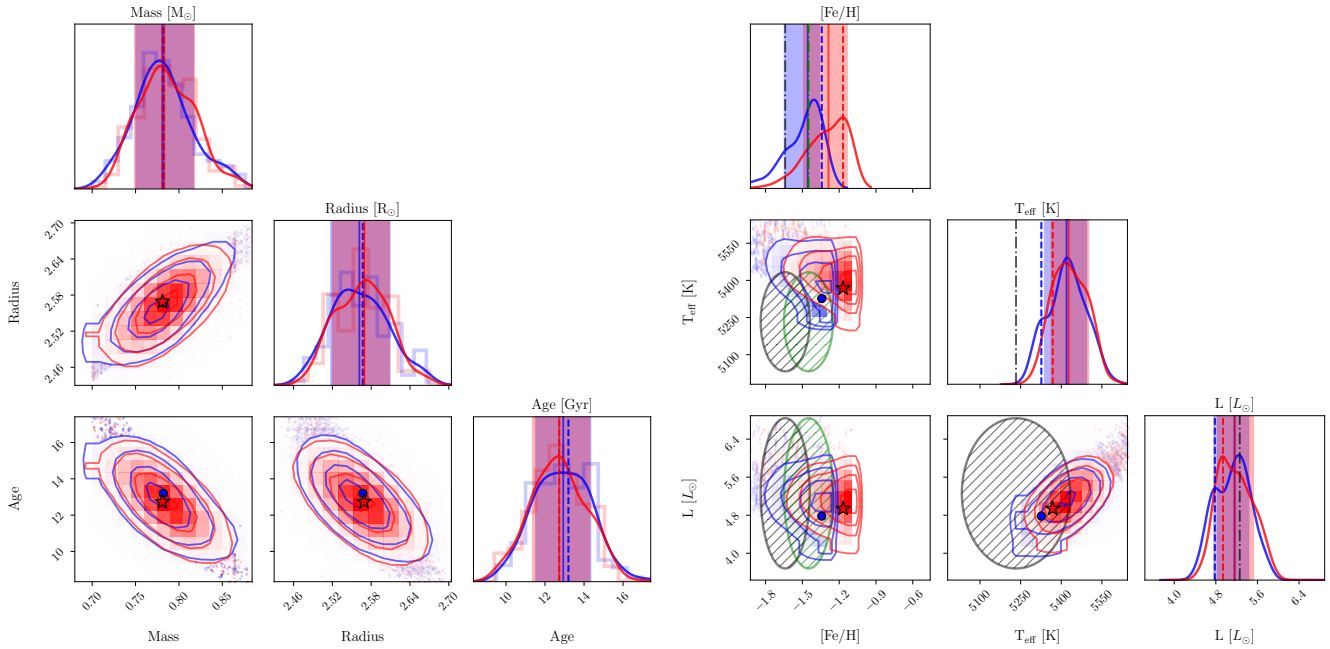

Figure 14. Same as Figure 10 except for KIC 7341231.

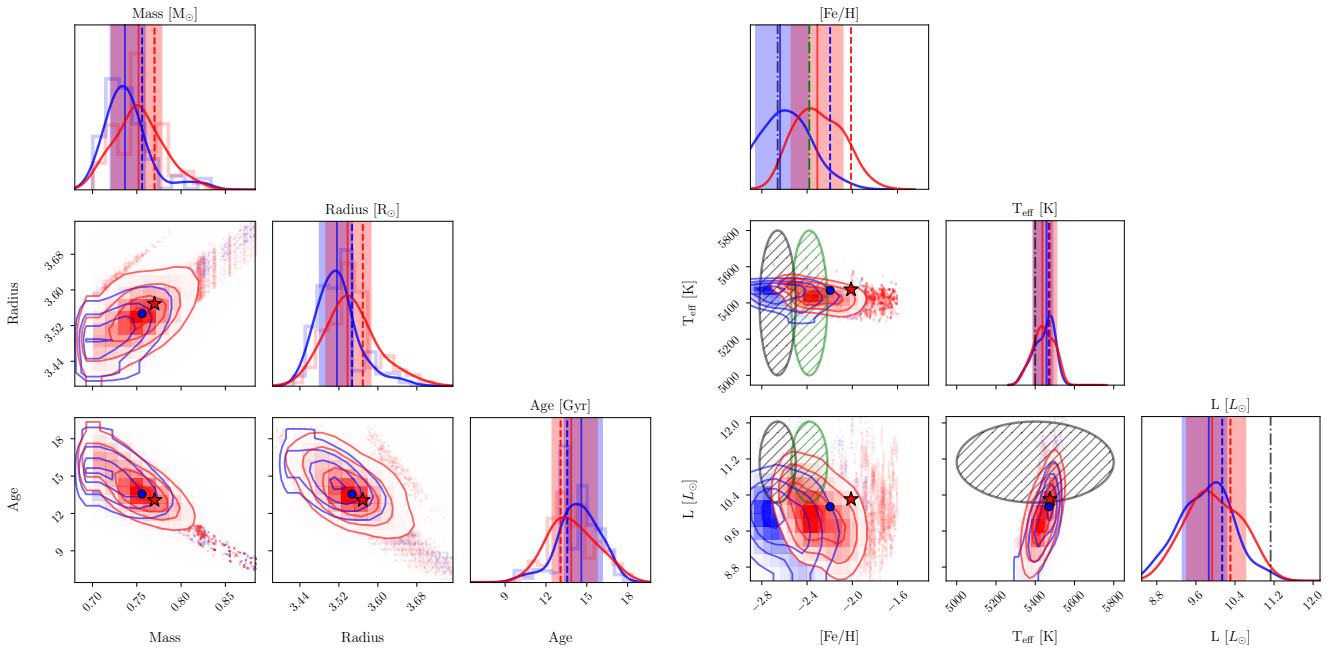

Figure 15. Same as Figure 10 except for KIC 8144907.

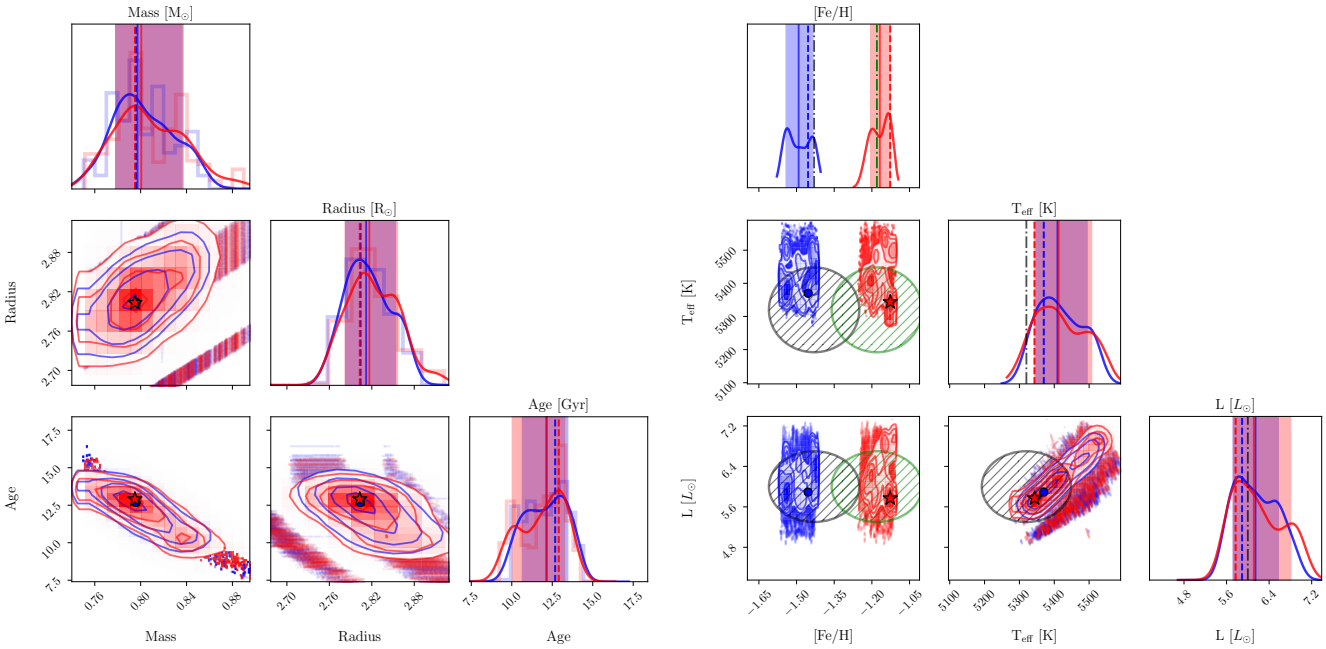

Figure 16. Same as Figure 10 except for ν Indi.